Biophysical modeling of preBötzinger Complex Type-1 Neuron

A Thesis

submitted to
Indian Institute of Science Education and Research Pune in partial
fulfilment of the requirements for the BS-MS Dual Degree Programme
by
Shivani Verma

Indian Institute of Science Education and Research Pune
Dr. Homi Bhabha Road,
Pashan, Pune 411008, INDIA.

March, 2024
Supervisor: Sufyan Ashhad
Shivani Verma

Certificate

This is to certify that this dissertation, entitled Biophysical modeling of preBötzinger Complex Type-1 neurons, represents the original work by Shivani Verma at the National Centre for Biological Sciences, TIFR Bangalore. This work was carried out under the supervision of Dr. Sufyan Ashhad, towards the partial fulfilment of the BS-MS dual degree program at the Indian Institute of Science Education and Research, Pune, during the academic year 2023-2024.

Sufyan Ashhad

Sufyan Ashhad

Committee:

Sufyan Ashhad

Suhita Nadkarni

This thesis is dedicated to the Breathing Neuroscience Laboratory and my family

Declaration

I hereby declare that the matter embodied in the report entitled Biophysical modeling of preBötzinger Complex Type-1 neuron is the result of the work carried out by me at the National Centre for Biological Sciences, TIFR Bangalore, under the supervision of Dr. Sufyan Ashhad, and has not been submitted elsewhere for any other degree. Wherever others contribute, every effort is made to indicate this clearly, with due reference to the literature and acknowledgment of collaborative research and discussions.

Shivani

Shivani Verma

20191127

Acknowledgments

I sincerely thank Dr. Sufyan Ashhad for allowing me to work on this project and for his guidance throughout this period. This work would not have been possible without his patience while I learned. His mentorship has been crucial for me to grow as a researcher. He has fascinated me with neuroscience. His support and positive attitude have always kept me motivated.

I thank Professor Suhita Nadkarni for her constructive feedback during my mid-year evaluation. Her continued mentorship has been pivotal for my academic progress.

I thank Professor Rishikesh Narayanan for letting me audit his neuronal physiology and plasticity course. This course has opened up many gates of my thinking, from a synapse to critically analyzing a paper—lifelong good practices in science.

I am grateful to the National Centre for Biological Sciences, TIFR, Bangalore, for accommodating me during my thesis period.

Contributions

Contributor name	Contributor role
Sufyan Ashhad and Shivani Verma	Conceptualization Ideas
Shivani Verma and Sufyan Ashhad	Methodology
-	Software
Shivani Verma and Sufyan Ashhad	Validation
Shivani Verma	Formal analysis
Shivani Verma	Investigation
Sufyan Ashhad	Resources
Shivani Verma	Data Curation
Shivani Verma	Writing - original draft preparation
Shivani Verma, Sufyan Ashhad and Breathing Neuroscience Lab members	Writing - review and editing
Shivani Verma	Visualization
Sufyan Ashhad	Supervision
Sufyan Ashhad	Project administration
Sufyan Ashhad	Funding acquisition

Contents

2.4 Parametric Ranges

2.5 Physiological measurement ranges

2.6 Making a preBötC Type -1 using MPMOSS

2.7 simulations and analysis

Chapter 3 Results

Chapter 4 Discussion

References

Appendix

Abstract

Breathing is a rhythmic motor behavior that regulates the exchange of blood gases. The preBötzinger Complex (preBötC) generates the inspiratory rhythm. preBötC rhythm is an emergent network property where synaptic connectivity and intrinsic neuronal properties play critical roles. Network synchronization in each breath cycle is necessary for preBötC rhythmogenesis. preBötC Type-1 neurons are putatively rhythmogenic. They synchronize with initial low-level activity due to convergent-coincident inputs from their pre-synaptic partners. However, we still lack an understanding of how preBötC Type-1 neurons can act as coincident detectors since the Type-1 neurons are considered integrators.

In this study, I developed experimentally constrained and validated models of preBötC Type-1 neurons to understand their physiology and computations. I constructed biophysical models of Type-1 neurons through a stochastic search spanning 24 model parameters and screened them for nine physiological measurements to ensure they were within their experimentally reported bounds.

Of over two lakh models, 135 models qualified as physiologically valid. We observed that degenerate interaction among model parameters gave rise to robust Type-1 phenotype and underlies their heterogeneity. Type-1 models exhibited a strong correlation between the A-type K + channel and the sodium persistent channel properties. Published single-cell (patch-sequencing) transcriptomics data validate this model prediction. Spike-triggered averaged currents of valid models revealed they span the entire spectrum of encoding regimes from integrators to coincidence detectors. We postulate that the heterogeneity in physiological and encoding characteristics of Type-1 neurons is crucial for the resilience and robustness of preBötC dynamics and breathing.

Synopsis

Breathing is a rhythmic motor behavior that regulates the exchange of blood gases in mammals and requires the coordinated activity of several muscles. These muscles are controlled by an intricate system of interconnected neural circuits, the breathing central pattern generator (bCPG) located in the brainstem. The preBötzinger Complex (preBötC) is the kernel of bCPG that generates the inspiratory rhythm. preBötC rhythm is an emergent network property where synaptic connectivity, network topology, and intrinsic neuronal properties play critical roles. However, existing preBötC models are based on pacemaker-like neurons and do not capture these emergent properties. The pacemaker-like currents are not necessary for preBötC rhythmogenesis as the rhythm persists when they are pharmacologically blocked. Recent studies revealed network synchronization in each breath cycle is necessary for preBötC rhythmogenesis. Further, electrophysiologically classified preBötC Type-1 neurons are putatively rhythmogenic and form the rhythmogenic kernel. These neurons fire sparsely in the inter-breath interval, but during the pre-inspiratory period, they start to synchronize, and activity builds up in the network. This pre-inspiratory activity transforms into an inspiratory burst. This transition from sparse firing to synchrony is the hallmark of Type-1 inspiratory neurons.

Type-1 neurons can synchronize with initial low-level activity due to convergent-coincident inputs from their pre-synaptic partners, which enable the recruitment of more neurons as the cycle progresses. However, we still lack an understanding of how preBötC Type-1 neurons can act as coincident detectors and participate in synchronization, given that, classically, Type-1 neurons are considered integrators. Since preBötC rhythm is an emergent network property, we must analyze interactions between intrinsic neuronal properties and synaptic connectivity to understand the mechanistic underpinnings of rhythm generation.

In this study, I developed experimentally constrained and validated models of preBötC Type-1 neurons to understand their physiology and computations. I constructed biophysical models of Type-1 neurons through a stochastic search spanning 24 model parameters related to voltage-gated ion channel properties, geometry, and passive electrical properties. These models were screened for nine physiological measurements of sub- and supra-threshold excitability to ensure they fell within their experimentally reported ranges. This strategy ensured we span a large parametric range without being biased towards hand-tuned models.

I simulated over two lakh models to search parametric combinations that give rise to preBötC Type-1 neurons. We found 135 models with physiological measurements within the experimental bounds and, thus, qualified as valid. These valid models captured the experimentally observed heterogeneity in preBötC Type-1 neurons. Most measurements were weakly correlated. Most model parameters were also weakly correlated, and most pairwise correlations between model parameters and measurements were also weak. When there was a correlation, one-to-many, and many-to-one correlation between the model parameters and measurements. Together, these findings suggest that degenerate interaction among model parameters gives rise to robust Type-1 phenotype in preBötC neurons and underlies their heterogeneity.

In the valid Type-1 neuronal models, we observed a strong correlation between the *A*-type K^+ channel and the sodium persistent channel properties*.* Thus, an important prediction from this study is that the A-type K+ channel and the sodium persistent channel must be correlated for the expression of the Type-1 physiological phenotype*.* This prediction is validated by the single-cell transcriptomics data available in the literature.

Having analyzed physiological determinants of preBötC Type-1 neurons, I explored their computational properties by computing spike-triggered averaged currents. We discovered that the preBötC Type-1 neurons span the entire spectrum of encoding regimes from integrators to coincidence detectors. We postulate that this wide range of physiological and encoding characteristics of Type-1 neurons is crucial for the resilience of the preBötC network and robustness of breathing under various physiological states.

The first step in understanding preBötC rhythmogenesis is to create biophysically realistic neuronal models; the second step is to connect them in a network to develop a quantitative framework for preBötC synchronization and rhythmogenesis. In this thesis, I implemented the first step of the work, which was to construct the Type-1 population. My future experiments will be to construct preBötC rhythmogenic microcircuit models by incorporating these neurons to understand the physiological mechanisms of breathing rhythmogenesis.

Chapter 1

Introduction

1.1 Breathing CPG

During Routine work, breathing occurs effortlessly and involuntarily. It is an essential rhythmic motor behaviour that drives gaseous exchange through the lungs. Under normal metabolic conditions, i.e., at rest, a breath has two components:

1. **Active inspiration** occurs when the diaphragm receives neuronal signals to contract and its downward movement leads to expansion and inhalation.
2. **Passive expiration** is driven by the diaphragm's recoil force. Under passive expiration, the abdominal, the major expiratory muscle, does not receive any neuronal signal. During high metabolic demands such as running, exercise, and swimming, expiratory muscles contract to expel air from the lung (Abraham et al., 2002).

This automatic breathing is due to the preBötzinger Complex (preBötC), a part of the ventral medullary respiratory group located in the brainstem. preBötC generates the inspiratory rhythm, seamlessly regulating it without a conscious effort. Generation and regulation of respiratory rhythm can be studied in slice preparation (Smith et al., 1990). A healthy brainstem slice from rodents containing preBötC and hypoglossal nerve (XIIn) can generate rhythm independently (Figure 1.1). preBötC neurons project to XIIn, which projects to the upper airways and tongue. It facilitates the upper airway patency during each inspiration. Thus, in brainstem slices, the XIIn activity can be considered equivalent to (fictive) inspiration. Despite this accessibility of neurons and network, understanding the rhythmogenic mechanisms has been challenging, mainly because of two reasons:

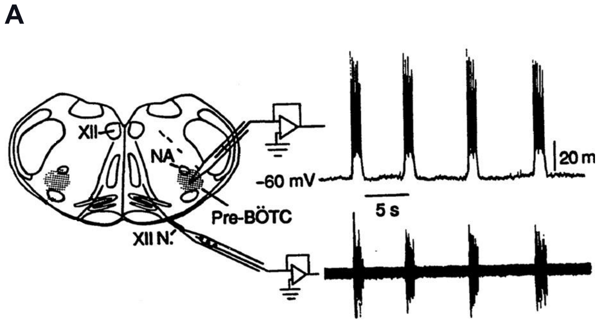

Figure 1.1. Brain Stem Slice Preparation to study inspiratory Rhythm. Simultaneous recordings from preBötC neurons and hypoglossal nerve(XIIn) showing aligned burst firing where each burst is equivalent to (fictive) inspiration. Figure adopted from (Smith et al., 1991).

1. The canonical central pattern generation mechanisms based on pacemaker neurons or half-center oscillators are not true for preBötC (Ashhad et al., 2022).
2. preBötC consists of diverse neuronal subpopulations based on their neurotransmitter types, electrophysiological properties, and molecular markers. Until recently, it was impossible to specifically target these neuronal subtypes

to understand their role in breathing rhythmogenesis. Now, transgenic mice lines are deployed to express fluorescent proteins specifically in subpopulations of neurons and record from them.

1.2 Neuronal Diversity

In initial attempts to understand the preBötC neuronal diversity, Rekling et al., 1996 carried out the electrophysiological recording to understand the electrophysiological

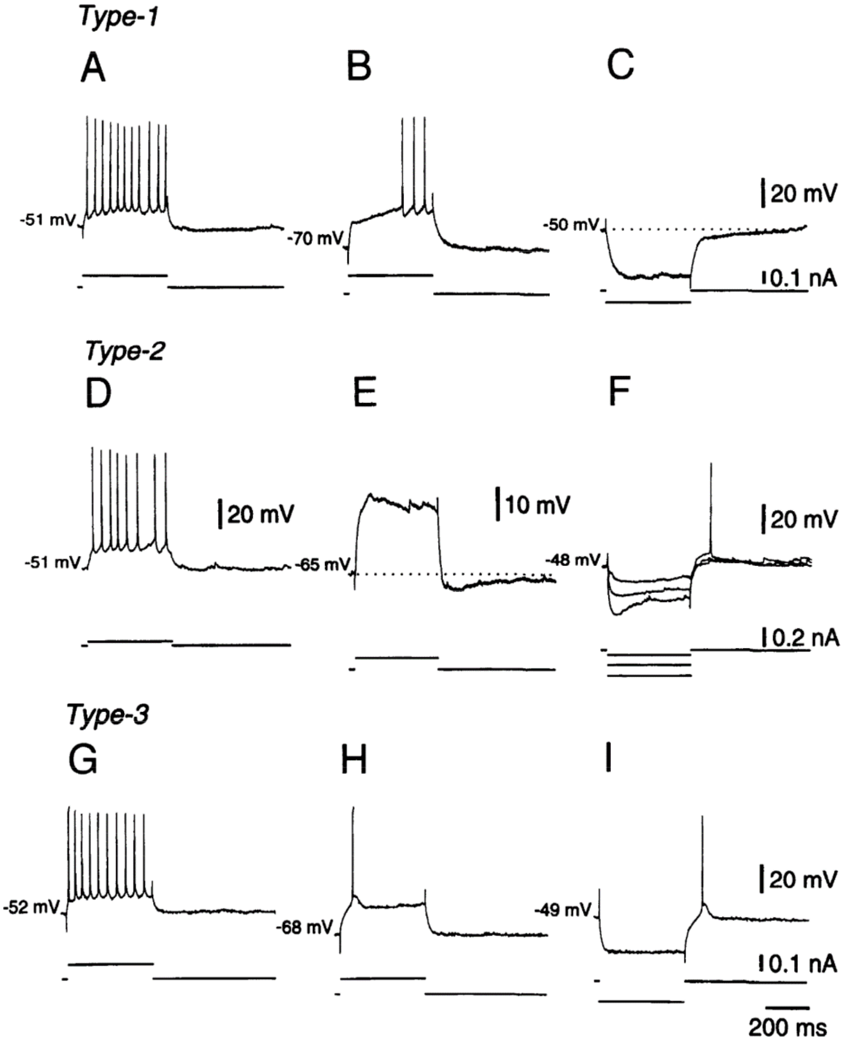

Figure 1.2. Electrophysiological classification of preBötC neurons:
Type-1: When these neurons are held at -70mV and given a depolarizing current, fire action potential after a delay known as latency to first spike.
Type-2: when these neurons are injected with a hyperpolarizing current pulse, they show an initial membrane potential drop that recovers partially due to the activation of hyperpolarization-activated cyclic nucleotide-gated (HCN) channels. This results in the sag potential.
Type-3: These neurons do not show firing or spike once until highly depolarized. With a hyperpolarizing current, they show a rebound spike.
Figure adopted from (Rekling et al., 1996)

diversity of neurons in preBötC. Based on the electrophysiological properties of preBötC Rekling et al., 1996, classified them into three classes: Type-1, Type-2, and Type-3 (Hodgkin, 1948). The initial latency to the first action potential firing is a prominent characteristic of preBötC Type-1 neurons (Figure 1.2). Type-2 neurons, on the other hand, are characterized by their sag potential. The sag potential arises due to HCN channels (Kallurkar et al., 2022). Lastly, Type-3 neurons are mostly silent when depolarized and show a rebound spike. Simultaneous preBötC neuron and XIIn recordings revealed that Type-1 neurons start firing at low-frequency before the onset of inspiration in each cycle (Gray et al., 1999) (Figure 1.3). The low-frequency firing by Type-I neurons starts at 398 ±102 ms (mean ± SD) before the onset of XIIn activity, whereas Type-2 has a smaller latency of onset at 171 ±87 ms (Rekling et al., 1996). This pre-inspiratory preBötC activity is also observed in multi-unit recordings in anesthetized rodents, suggesting that it is crucial to generate preBötC rhythm.

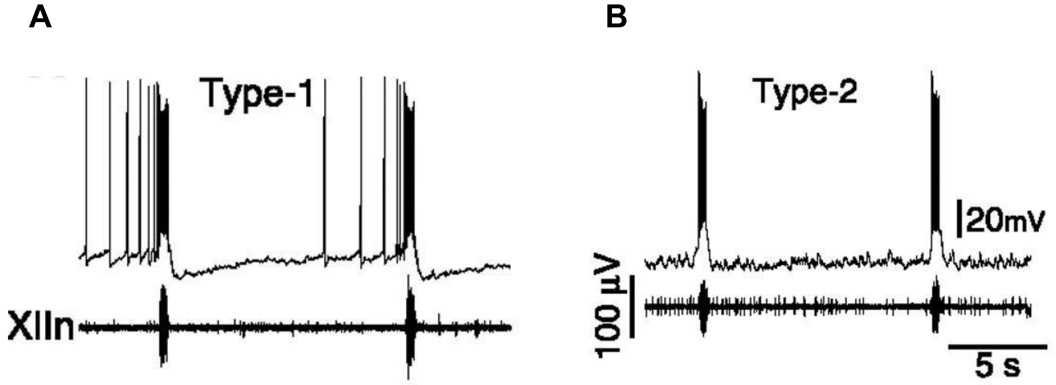

Figure 1.3. Activity of preBötC neurons during inspiratory rhythms. Simultaneous recording of Type-1 or Type-2 neurons with XIIn. (A) Type-1 neurons show low-frequency firing before the onset of Inspiration in XIIn, Whereas (B) Type-2 firing is aligned with Inspiratory bursts in XIIn. Figure adopted from (Gray et al., 1999)

With this understanding of electrophysiological diversity in the preBötC neurons, subsequent papers explored their molecular identity. To figure out the developmental origin of the preBötC rhythmic network (Bouvier et al., 2010) employed transgenic mouse lines and found that the transcription factor Developing brain homeobox 1 (Dbx1) gene controls the fate of glutamatergic interneurons of preBötC. Dbx1+ neurons means the neurons that expressed Dbx1 developmentally. This is because postnatal preBötC neurons do not express Dbx1. Ablation of Dbx1 expressing neurons (hereafter referred to as Dbx1+ neurons) completely silenced the preBötC and caused a massive loss of preBötC glutamatergic neurons. Further, *Dbx1* null mutant had a beating heart but did not show breathing movement and died within minutes of delivery. Electrophysiological recordings showed that Dbx1+ neurons exhibit excitatory Type-1 and Type-2 properties (Figure 1.4) (Picardo et al., 2013). Type-1 neurons are the excitatory population of the preBötC, and they start firing in the pre-inspiratory (pre-I) period. This suggests that Type-1 activity might be a deciding factor in inspiratory rhythmogenesis and that it may constitute the rhythmogenic preBötC population. To test this hypothesis, (Cui et al., 2016) expressed Channelrhodopsin-2 (ChR2) in the $Dbx1^{+}$neurons. Photo-stimulation of these neurons induced the next inspiration onset earlier than expected (Figure 1.5A). This experiment was repeated at various times spanning two consecutive inspirations, and the phase shift (ratio of perturbed cycle duration to control cycle duration) was calculated. Photo-stimulation of $Dbx1^{+}$neurons caused phase advancement in breathing rhythm.

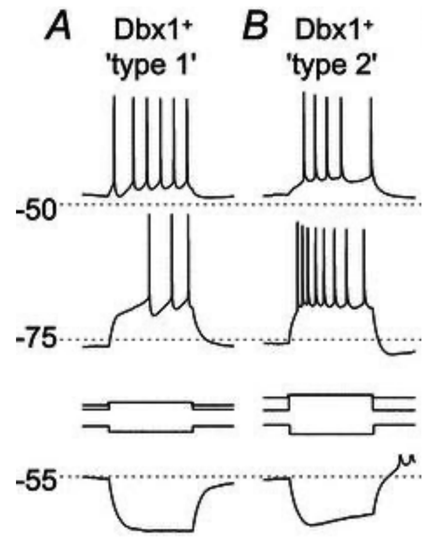

Figure1.4. Delayed excitation and sag potential in Dbx1⁺ neurons. Type-1 Dbx1⁺ neurons exhibit delayed excitation upon depolarizing current injection and no sag potential in response to the hyperpolarizing current pulse. Type-2 $Dbx1^{+}$ neurons exhibited sag potential. Figure adopted from (Picardo et al., 2013)

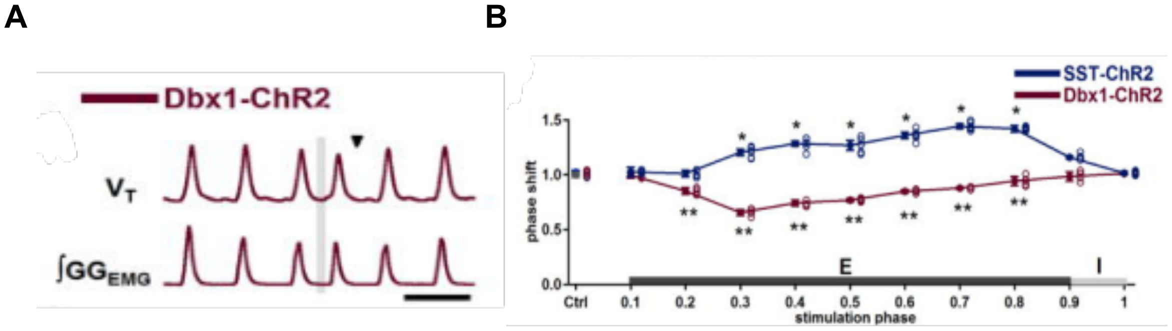

Figure 1.5. Dbx1+ photostimulation leading phase advancement in inspiration onset. (A) Photostimulation (indicated in grey bar) of Dbx1+ ChR2 in preBötC between two inspiration leads to early onset of inspiration (black arrow) indicated in V_T (tidal volume) and in genioglossus electromyographic activity (GG_{EMG}) and Dbx1+ ChR2 V_T. (B) Phase shift curve with respect to stimulation at different phases of expiration (phase: 0.0–0.8) or inspiration (phase: 0.9–1.0). Electromyographic activity (GG_{EMG}) measures the electrical activity of the muscle in response to nerve stimulation. Figure adopted from (Cui et al., 2016)

The $Dbx1^+$population can be divided into somatostatin expressing (SST+) and non-expressing (SST-) subpopulations. Photo-stimulation of SST+ neurons, prominently Type-2 (Ashhad and Feldman, 2020), did not lead to phase advancement, suggesting that Type-1 neurons are critical for setting the phase advancement. This lends itself to further evidence for the Type-1 population being rhythmogenic. This series of experiments confirms that the Dbx1+ neurons form glutamatergic Type-1 and Type-2 populations, with Type-1 neurons being putatively rhythmogenic.

To summarise, the preBötC neuronal population can be functionally segregated into rhythmogenic and patternogenic neurons, comprising Type-1 and Type-2 neurons, respectively (Figure 1.6). However, mechanistic understanding of rhythm generation is not well established. Multiple research groups have tried to explain the rhythm generation by making network models with high calcium levels to activate calcium-activated cation-non-specific currents (CAN) and persistent sodium (Nap) -dependent bursting. While persistent sodium depolarises the neurons activating CAN, Nap time-dependent inactivation leads to termination of the activity. This cycle repeats and hypothesized to explain the preBötC rhythm (Butera et al., 1999; Phillips and Rubin, 2022). However, these models don't hold up under physiological conditions without evidence of such calcium levels in physiological scenarios and no evidence of pacemaker neurons in preBötC. Theoretical models built around these hypotheses show bursting driven by Nap and CAN currents and match the output of the preBötC network. However, these models cannot explain the physiological mechanisms underlying preBötC rhythmogenesis (Butera et al., 1999).

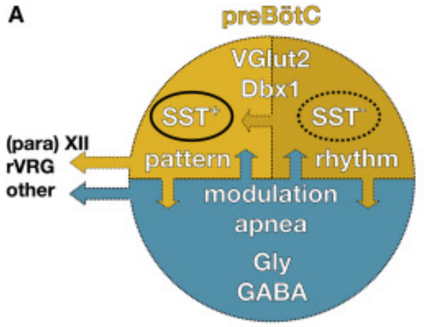

Figure 1.6. preBötC neuronal diversity. Dbx1$^+$ population of the preBötC is excitatory and can be divided into SST$^+$ and SST$^-$ neurons, which are patternogenic (Yan Cui et al., 2016) and putatively rhythmogenic populations, respectively. About half of the preBötC population consists of inhibitory neurons. Figure adopted from (Ashhad and Feldman, 2020)

The alternative framework for rhythmogenesis came from the Burstlet Theory.

Type-1 neurons exhibit low levels of gradually increasing ensemble activity before inspiratory bursts (when the whole network synchronizes to generate a population burst) during pre-inspiration. The Burstlet Theory proposes that this pre-inspiratory activity represents the latent signature of an emerging mechanism for rhythmogenesis. When excitability is high, inspiratory bursts consistently occur with highly synchronized activity in each preBötC cycle, driving motor output. Whereas under lowered excitability, expected XIIn bursts may not manifest at the expected times due to low synchrony firing in the preBötC rhythmogenic population. Instead, rhythmic bouts of synchronous low-level population activity, termed burstlets, appear within the preBötC. The absence of expected XIIn bursts is due to the failure of the burstlet to trigger inspiratory bursts that would normally propagate to motor neurons (Figure 1.6). To understand how preBötC synchronizes and the factors that govern burstlet to burst conversion, Ashhad & Feldman, 2020 simultaneously recorded from pairs of output neurons (Type-2) and discovered that excitatory postsynaptic potentials onto these pairs (which are the inputs from their presynaptic partners/ rhythmogenic neurons)

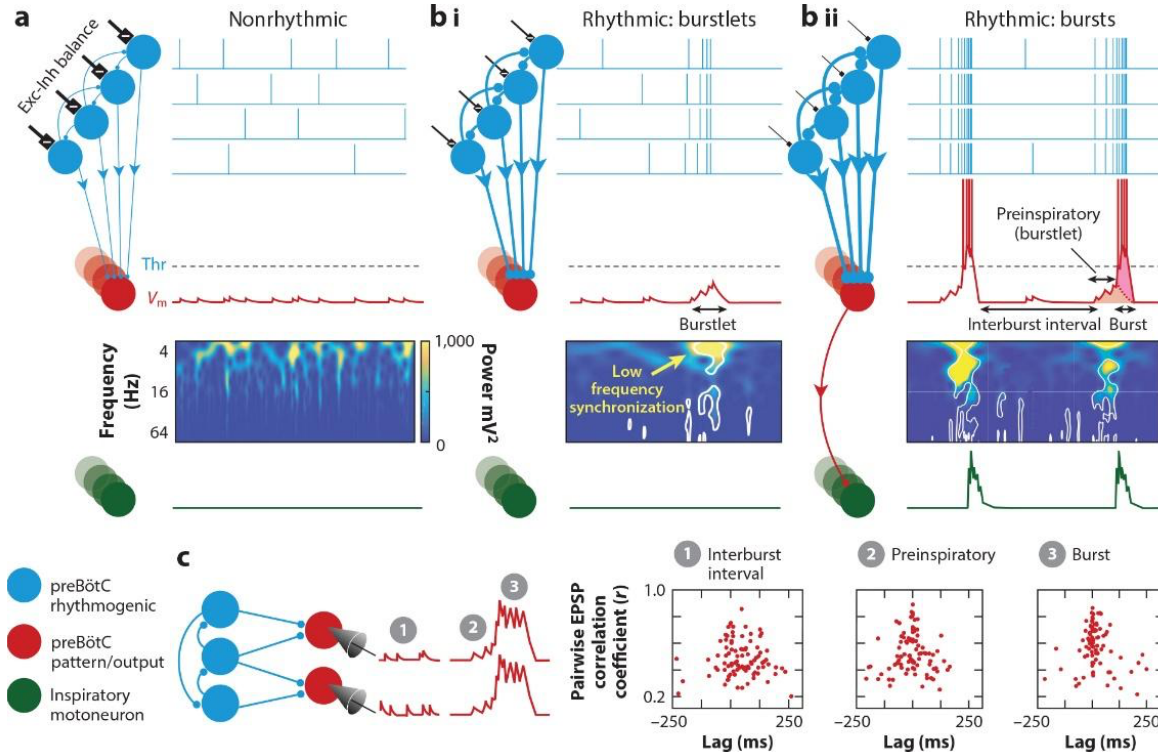

Figure 1.7 preBötC rhythmogenesis. The preBötC keeps the rhythmic breathing going by syncing up its neurons, controlled by the balance of excitation and inhibition (E-I) in the network. In scenario (a), when the E-I balance is shifted towards inhibition, the rhythmogenic neurons fire but can't synchronise, resulting in no rhythm. In (b), with more excitation, the neurons start synchronizing. This synchronization increases the activity in the output neurons, indicating the emergence of the rhythm. As excitation keeps increasing, neuronal synchronization gets stronger until it reaches a tipping point, leading to an inspiratory burst that is relayed to the (pre) motor neurons via the preBötC output neurons. (c)The synchrony among neurons is evident in their membrane potential correlograms, revealing increased temporal alignment of synaptic inputs onto the pairs of output neurons during the preinspiratory periods and inspiratory bursts. Figure adopted from (Ashhad et al., 2022)

show lesser and lesser correlation lags as the cycle progresses from interburst intervals to pre-inspiratory period and inspiratory bursts (Figure 1.6). This revealed the progressive synchronization of the rhythmogenic population during inspiratory burst formation. When this synchrony was low, preBötC activity terminated as a burstlet.

The follow-up modeling study (Ashhad et al., 2023) revealed that for the preBötC to synchronize in every cycle, based on physiological constraints, the network must operate as a coincident detector. Specifically, Type-1 neurons can synchronize from initial low-level activity due to convergent-coincident inputs from their pre-synaptic partners that enable the recruitment of more and more neurons as the cycle progresses. However, we still lack an understanding of how preBötC Type-1 neurons can act as coincident detectors and participate in synchronization, especially given that, classically, Type-1 neurons are considered as integrators (Prescott, 2014). preBötC rhythm appears to be an emergent network property, we must analyze interactions between intrinsic neuronal properties and synaptic connectivity to understand the mechanistic underpinnings of rhythm generation. Thus, it is crucial to construct preBötC network models with biophysical models of Type-1 neurons, whose properties faithfully cover the range of physiological measurements from experiments. The first step in understanding preBötC rhythmogenesis is to create biophysically realistic neuronal models; the second step is to connect them in a network to develop a quantitative framework for preBötC synchronization and rhythmogenesis. In this thesis, I have focused on the first step: creating a biophysical neuronal population of preBötC Type-1 neurons to understand their physiology and computations.

Chapter 2

Methods

For constructing Biophysical models of Type-1 neurons, it is necessary to know the ion channel expression in these neurons. An ion channel is made up of multiple subunits. Different genes can encode functionally equivalent subunits. Hence, the same functional ionic current can be mediated by channels of different subunits, giving rise to different properties in different neuron types in different brain regions.

With this understanding, we constructed the phenomenological ion channel models of effective currents/conductance of various types instead of applying the activity of ion channels with biologically accurate subunits. We used experimental data from the literature for preBötC ion channels and made eight ion channels discussed in 2.2. We employed Hodgkin and Huxley formalism to construct the ion channels of the preBötC Type-1 neuron.

2.1 Hodgkin and Huxley Model

Hodgkin and Huxley used the squid giant axon, a simple system to understand the neuron's electrical properties and action potential generation. Using a parallel conductance model, they characterized sodium and potassium currents and explain action potential generation and propagation in the neuron, represented as an RC circuit (Hodgkin and Huxley 1952).

Each component of the cell is represented as an electrical component. The lipid bilayer is defined as a capacitor, voltage-gated ion channels as conditional resistors, and electrochemical gradient as a voltage source whose voltage is determined by relative concentrations of the ion species inside and outside the cell.

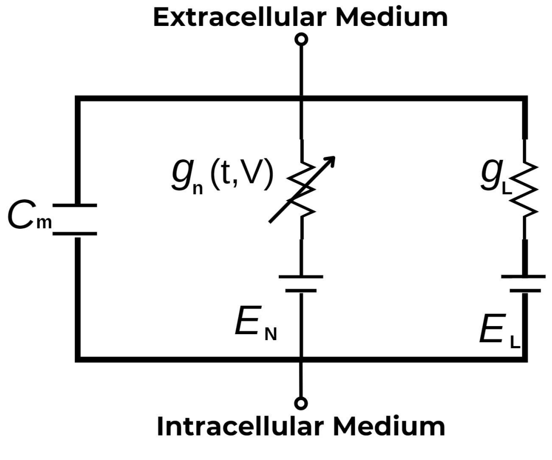

Figure 2.2. Neuron as RC circuit where ion channel is represented as conditional resistor, lipid membrane layer as capacitor. Voltage source is the reversal potential of the ion across the membrane for that particular ion channel (E_N).

This model consists of a set of differential equations, explained below:

Mathematically, the cell lipid bilayer acts as a capacitor because it separates the charges and thus, is represented as capacitor in the diagram. The capacitive current through the lipid bilayer is given by:

$$I_c = \frac{C_m \, dV_m}{dt} \tag{1}$$

where V_m is the membrane voltage and C_m is the specific capacitance of the cell.

An ion channel acts as a resistor because it offers resistance to the current that flows through the membrane. Current through an ion channel is given by

$$I_i = g_i(V_m - E_i) \tag{2}$$

Where E_i is reversal potential of the ion, g_i is the conductance of the ion channel.

Current through the membrane can be written as the summation of capacitive and ionic currents.

$$I = I_c + I_i \tag{3}$$

$$I = \frac{C_m \, dV_m}{dt} + g_i(V_m - E_i) \tag{4}$$

Each ion channel is represented as a separate conditional resistor in the cell. A cell with sodium and potassium channels can be represented as below

$$I = \frac{C_m dV_m}{dt} + g_k(V_m - E_k) + g_{Na}(V_m - E_{Na}) + g_l(V_m - E_l) \tag{5}$$

In our model of Type-1 neurons, we incorporated eight ion channels mentioned in section 2.2. Ion channels are functions of both time and voltage; this dependence is represented using gating variables equation 6:

$$I = \frac{C_m dV_m}{dt} + \bar{g}_{kdr}a^4(V_m - E_k) + \bar{g}_{Na}a^3 i(V_m - E_{Na}) + \bar{g}_{KA}ai(V_m - E_k) + \bar{g}_{Nap}ai\big(V_m - E_{Nap}\big) + \bar{g}_{CaSK}a^2(V_m - E_k) + \bar{g}_{CaT}a^2 i\left(1 - \frac{Ca_i}{Ca_o}\right) + \bar{g}_{CaL}ai(Ca_i)\left(1 - \frac{Ca_i}{Ca_o}\right) + \bar{g}_{CAN}a(Ca_i)(V_m - E_{CAN}) + \bar{g}_l(V_m - E_l) \tag{6}$$

Where a represents the activation and i represents inactivation of ion channel. $\underline{g}_k$, $\underline{g}_{Na}$, $\underline{g}_{KA}$, $\underline{g}_{Nap}$, $\underline{g}_{CaSK}$, $\underline{g}_{CaT}$, $\underline{g}_{CaL}$, $\underline{g}_{CAN}$, $\underline{g}_l$ are the conductance's at steady state of eight ion channels used in our model.

$$\frac{dx}{dt} = \frac{x_\infty - x}{\tau_x} \qquad (7)$$

Where x can be an activation (a) or inactivation (i) variable

$$x_\infty = \frac{\alpha_x}{\alpha_x + \beta_x} \qquad (8)$$

$$\tau_x = \frac{1}{\alpha_x + \beta_x} \qquad (9)$$

α_x , β_x are activation/inactivation rate constants of an ion channel transitioning from open to close, and vice versa. x is activation/inactivation variable associated with a channel and τ_x is the time constants of the activation/inactivation variable.

Ion channel dynamics can be understood via three curves: activation probability, inactivation probability and time constant. The activation/inactivation curves a_∞/i_∞ show the probability of a channel to open/close as a function of voltage. The time constant ($\tau_{a/i}$) curve shows how fast the channel activates/inactivates as a function of voltage. Varying the properties ($V_{1/2}\ Activation,\ V_{1/2}\ Inctivation, \tau\ Max$) (Constants) of these curves change the ion channel dynamics Figure 2.3. This is the strategy we used to span the reported ranges for our stochastic and unbiased search.

2.2. preBötC Type-1 Neuronal Ion Channels

2.2.1. Sodium Fast Channel

This channel replicates the fast sodium current of the preBötC. Because of its fast kinetics, it is also called transient sodium channel. It activates within a few milliseconds of current injection in a voltage-dependent manner. We used the experimental data reported by (Rybak et al., 2003) for preBötC Sodium transient currents. Equations used to construct it are as follows:

$$I = \bar{g}_{Na} a^3 i (V_m - E_{Na}) \qquad mA/cm^2 \qquad (10)$$

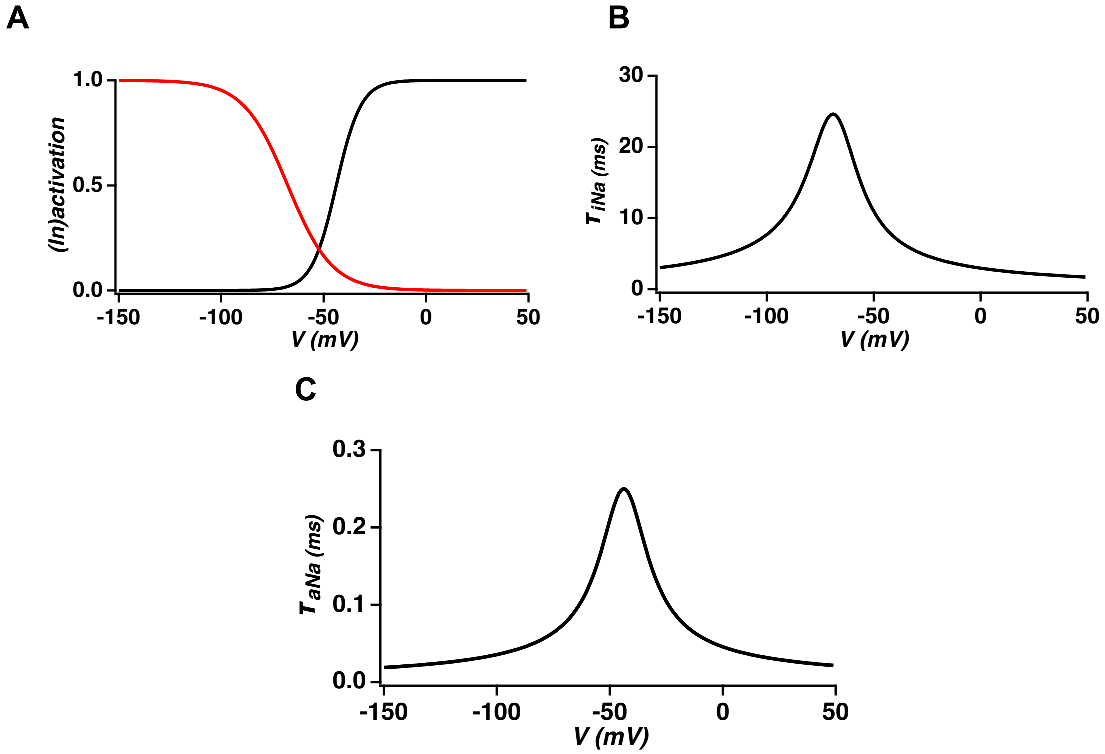

Figure 2.4. Sodium fast kinetics constructed from the experimental data (A) shows activation ($m_{\infty Na}$) and inactivation ($h_{\infty Na}$) probabilities of the sodium channel with respect to voltages. (B) shows activation time constant (τ_{mNa})of the sodium channel with respect to voltages. (C) shows inactivation time constant (τ_{hNa})of the sodium channel with respect to voltages.

$$\frac{dx_{a/i}}{dt} = \frac{x_{a/i\,\infty} - x_{a/i}}{\tau_{a/i}} \tag{11}$$

$$\tau_{a/i} = \frac{1}{qt(\alpha_{a/i} + \beta_{a/i})} \qquad ms \tag{12}$$

$$x_{a/i\,\infty} = \frac{1}{1 + exp^{-\frac{V_m - V_{a/i\,\frac{1}{2}}}{k_{a/i}}}} \tag{13}$$

where, i) $V_{a/i\,\frac{1}{2}}$ is the value of voltage at which activation or inactivation of a channel is 50%,

ii) $k_{a/i}$ is the factor that defines the slope of $x_{a/i\,\infty}$ the activation or inactivation probability curve (A)

iii) $\alpha_{a/i}$, $\beta_{a/i}$ are rate constants for an ion channel to make transitions from open to close and vice versa.

iv)$\tau_{a/i}$ is the time constants of the sodium activation/inactivation.

v) $x_{a/i\,\infty}$ is the function that produces the voltage dependent activation/inactivation probability.

2.2.2. *T*-Type Calcium Channel

These are low voltage-activated calcium channels activated at hyperpolarized voltages , also called transient opening calcium channels. We used the experimental data and curves reported by (Elsen and Ramirez, 1998)

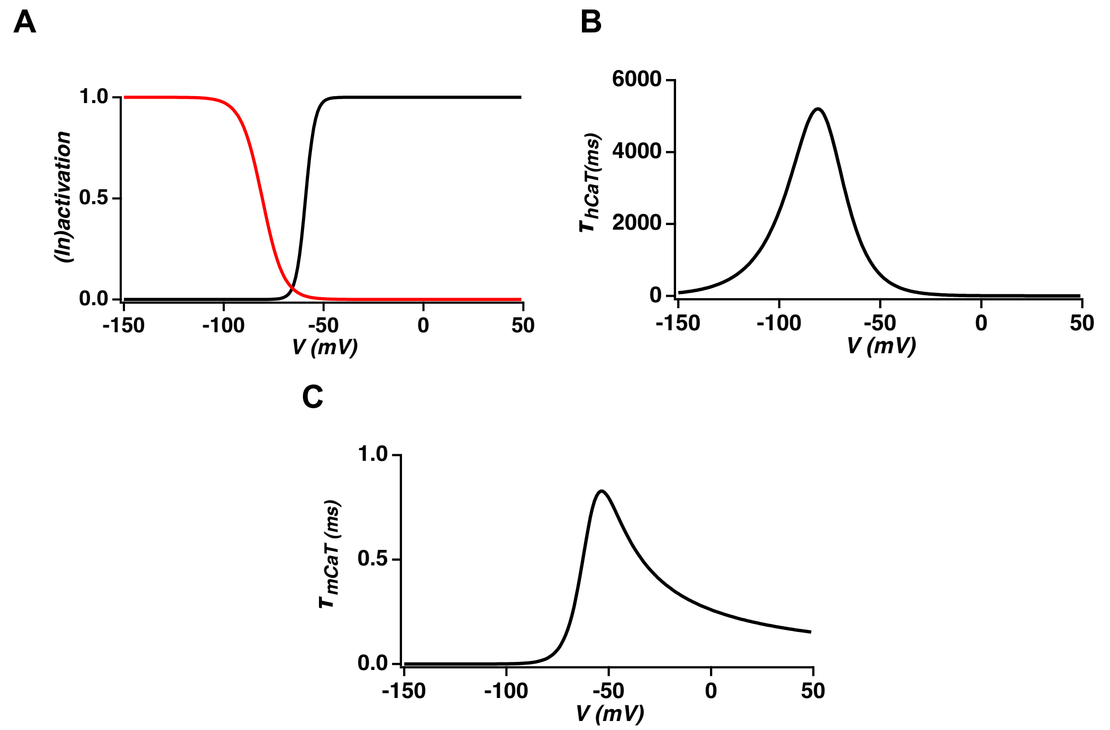

Figure 2.5. T type calcium channel kinetics (A) shows activation ($m_{\infty CaT}$) and inactivation ($h_{\infty CaT}$) probabilities of the T type channel with respect to voltages. constructed from the data Ramirez and Elsen 1998 (B) shows activation time constant (τ_{mCaT})of the *T*-type channel with respect to voltages. constructed without experimental data (C) shows inactivation time constant (τ_{hCaT})of the T type channel with respect to voltages constructed without experimental data.

$$I = \bar{g}_{CaT} a^2 i \left(1 - \frac{Ca_i}{Ca_o}\right) \qquad (14)$$

$$\frac{d(a/i)}{dt} = \frac{a/i_{\infty CaT} - a/i}{\tau_{a/iCaT}} \qquad (15)$$

$$\tau_{a/i\;CaT} = \frac{1}{C(\alpha_{a/i} + \beta_{a/i})} \qquad (16)$$

$$a/i_{\infty CaT} = \frac{1}{1+exp^{-\frac{V_m - V_{a/i\,1/2CaT}}{k_{a/i\,CaT}}}} \tag{17}$$

$$\alpha_a = \frac{0.055(V_{a1/2CaT} - V_m)}{exp^{-\frac{V_{a1/2CaT} - V_m}{k_{aCaT}}} - 1} \tag{18}$$

$$\beta_a = 0.94 exp^{\frac{V_{a1/2CaT} - V_m}{5.5}} \tag{19}$$

$$\alpha_i = 1.6e^{-4} exp^{-\frac{V_m - V_{i1/2CaT}}{k_{iCaT}}} \tag{20}$$

$$\beta_i = \frac{1}{exp^{-\frac{-V_m + V_{i1/2CaT}}{k_{iCaT}}} + 1} \tag{21}$$

Where,

α_a, β_a, α_i and β_i are rates of transitions of open to close and vice versa of activation and inactivation of calcium activated calcium permeable channel T-type Calcium channel (CaT). $\tau_{a/iCaT}$ is the time constants of the T channel activation/inactivation. $a/i_{\infty CaT}$ is the function that produces the voltage dependent activation/inactivation probability. $V_{a/i1/2CaT}$ is the value of voltage at which activation or inactivation of a channel is 50% where as $k_{a/iCaT}$ is the factor that defines the slope of $a/i_{\infty CaT}$ the activation or inactivation probability curve.

2.2.3. *L*-Type Calcium Channel

These are high voltage activated calcium channels activated at more depolarized voltages, also called long lasting calcium channels. We used the experimental data reported in (Elsen and Ramirez, 1998).

$$I = \bar{g}_{CaL} ai(Ca_i)\left(1 - \frac{Ca_i}{Ca_o}\right) \tag{22}$$

$$\frac{da}{dt} = \frac{a_{\infty CaL} - a}{\tau_{aCaL}} \tag{23}$$

$$a_{\infty CaL} = \frac{1}{tfa(\alpha_a + \beta_a)} \tag{24}$$

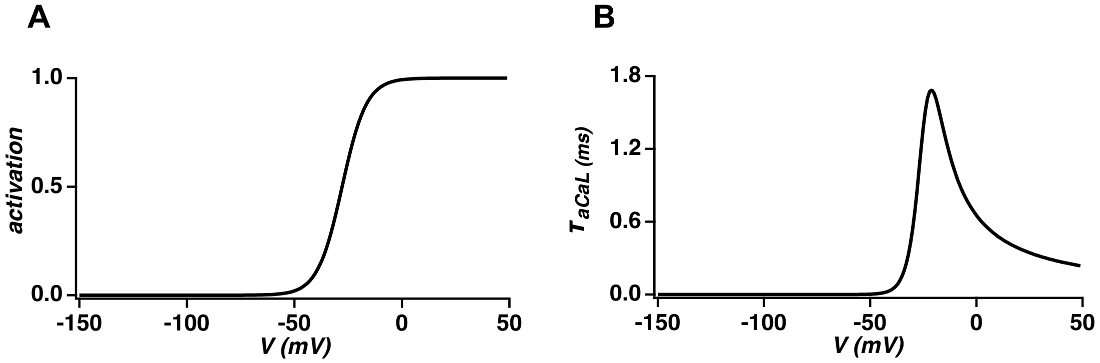

Figure 2.6. L type calcium channel kinetics (A) shows activation ($n_{\infty CaL}$) probability of the L type channel with respect to voltages. constructed from the data Ramirez and Elsen 1998 (B) shows activation time constant (τ_{nCaL})of the L type channel with respect to voltages. constructed without experimental data.

$$\tau_{aCaL} = \frac{\alpha_a}{\alpha_a+\beta_a)} \tag{25}$$

$$i(Ca_i) = \frac{C}{C+Ca_i} \tag{26}$$

$$\alpha_a = \frac{0.055(V_{a1/2CaL}-V_m)}{exp^{-\frac{V_{a1/2CaL}-V_m}{k_{aCaL}}}-1} \tag{27}$$

$$\beta_a = 0.94exp^{\frac{V_{a1/2CaL}-V_m}{5.5}} \tag{28}$$

Where,

α_a, β_a are rates of transitions of open to close and vice versa of activation of calcium activated calcium permeable channel *L*-type Calcium channel (CaL). τ_{aCaL} is the time constants of the L channel activation. $a_{\infty CaL}$ is the function that produces the voltage dependent activation probability. $V_{a1/2CaL}$ is the value of voltage at which activation or inactivation of a channel is 50% where as k_{aCaL} is the factor that defines the slope of $a_{\infty CaL}$ the activation probability curve.

$V_{a1/2CaL}$= –27.82 mV

k_{aCaL} =5.6

tfa =5

2.2.4. *A*-type Potassium Channel

This is voltage dependent potassium channel with quite fast kinetics such that it completes with fast sodium channel. This is one of the main channels that plays a major role in the Type-1 phenotype of preBötC. During the initial latency period, it competes with fast sodium and firing starts only after it starts to inactivate and sodium current takes over. We used the experimental data and curves reported by (Hayes et al., 2008)

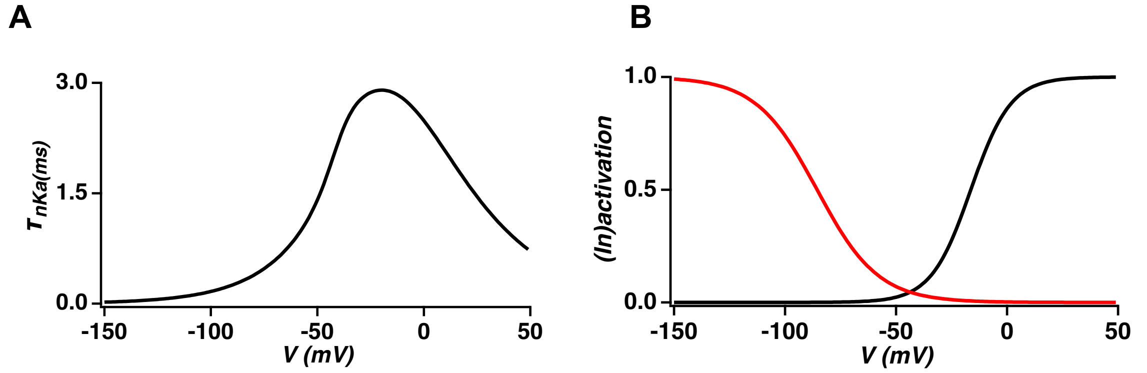

Figure 2.7. ***A*-type potassium channel kinetics** (A) shows activation (n_∞^{KA}) and inactivation ($I_{\infty Ka}$) probabilities of the A type potassium channel with respect to voltages. constructed from the data Hayes et al., 2008 (B) shows activation time constant (τ_{nKa}) of the *A*- type channel with respect to voltages. constructed with experimental data. (τ_{IKa}) is constant $\tau_{lKA} = 250\ ms$.

$$I = \bar{g}_{KA} a i (V_m - E_k) \tag{30}$$

$$\frac{d(a/i)}{dt} = \frac{a/i_{\infty KA} - a/i}{\tau_{a/iKA}} \tag{31}$$

$$a/i_{\infty KA} = \frac{1}{exp^{-\frac{V_m - V_{a/i1/2KA}}{k_{a/iKA}}} + 1} \tag{32}$$

$$\tau_{aKA} = \frac{mfac * \beta_a}{qt * a(\alpha_a + 1)} \tag{33}$$

$$\tau_{iKA} = 50 * ifac \tag{34}$$

$$Z = \frac{-1.5 - 1}{1 + exp^{\frac{V_m + 40}{5}}} \tag{35}$$

$$\alpha_a = \frac{exp^{-\frac{1e^{-3} Z \left(V_m - V_{m1/2KA}\right) 9.648 e^4}{k_{mKA}}}}{8.315(273.16 + celsius)} \tag{36}$$

$$\beta_a = \frac{exp^{-\frac{1e^{-3} Z * gmn \left(V_m - V_{a1/2KA}\right) 9.648 e^4}{k_{aKA}}}}{8.315(273.16 + celsius)} \tag{37}$$

α_a, β_a are rates of transitions of open to close and vice versa of activation of *A*-type potassium channel. τ_{aKA} is the time constants of the KA channel activation/inactivation. $a/i_{\infty KA}$ is the function that produces the voltage dependent activation/inactivation probability. $V_{a1/2KA}$ is the value of voltage at which activation or inactivation of a channel is 50% where as k_{aKA} is the factor that defines the slope of $a/i_{\infty KA}$ the activation or inactivation probability curve.

a =0.05 (constant factor)

$qt = 3^{(celsius-22)/10}$ (factor to account for temperature variability)

$V_{i1/2KA}$=-85.6 (variable)

$V_{a1/2KA}$=-16.3 (variable)

gmn =0.55

k_{aKA}=14.9 (variable)

k_{iKA}=-13.8 (variable)

$afac$ =1 (variable)

$ifac$ =4 (variable)

2.2.5. Sodium Persistent Channel

This current is called persistent because of its large inactivation constant which is time dependent and voltage independent. In Type-1 of preBötC these channels always have non zero probability of opening at depolarized current. We used the experimental data and curves reported by (Yamanishi et al., 2018)

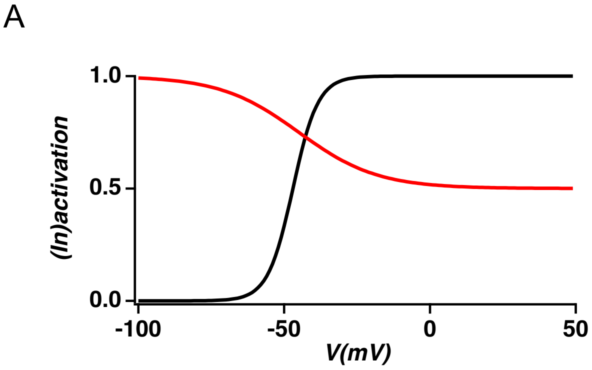

Figure 2.8. Sodium persistent channel kinetics (A) shows activation ($a_{\infty Nap}$) and inactivation ($i_{\infty Nap}$) probabilities of the persistent channel with respect to voltages. constructed from the data Yamanishi et al., 2018.

$$I = \bar{g}_{Nap} ai\left(V_m - E_{Nap}\right) \quad (38)$$

$$\frac{d(a/i)}{dt} = \frac{a/i_{\infty Nap} - a/i}{\tau_{a/iNap}} \quad (39)$$

$$a_{\infty Nap} = \frac{1}{exp^{-\frac{V_m - V_{a1/2Nap}}{k_{aNap}}} + 1} \quad (40)$$

$$i_{\infty Nap} = \frac{0.5}{exp^{-\frac{V_m - V_{i1/2Nap}}{k_{iNap}}} + 1} + 0.5 \quad (41)$$

$$\tau_{aNap} = 3 * afac \quad (42)$$

$$\tau_{iNap} = 571 * ifac \quad (43)$$

τ_{aNap} , τ_{iNap} are time constants of the KA channel activation/inactivation. $a_{\infty Nap}$, $i_{\infty Nap}$ are the function that produces the voltage dependent activation/inactivation probability. $V_{a1/2Nap}$, $V_{i1/2Nap}$ are the value of voltage at which activation/inactivation of a channel is 50% where as k_{aNap} , k_{iNap} is the factor that defines the slope of $m_{\infty Nap}$, $h_{\infty Nap}$ the activation/inactivation probability curve.

$V_{a1/2Nap}$=-47 (variable)

$V_{i1/2Nap}$=-39 (variable)

k_{aNap}=4.3

k_{iNap}=-9.5

afac =1 (variable)

ifac =1 (variable)

2.2.6. Delayed Rectifying Potassium Channel

No experimental data was available that characterized this channel in Type-1 of preBötC. We used data available for the hippocampal channels for our model (Mishra and Narayanan).

$$I = \bar{g}_{kdr} a^4 (V_m - E_k) \quad (44)$$

$$\frac{da}{dt} = \frac{a_{\infty kdr} - a}{\tau_{akdr}} \quad (45)$$

$$a_{\infty Kdr} = \frac{1}{exp^{\frac{V_{a1/2Kdr}-V_m}{k_{aKdr}}}+1} \qquad (46)$$

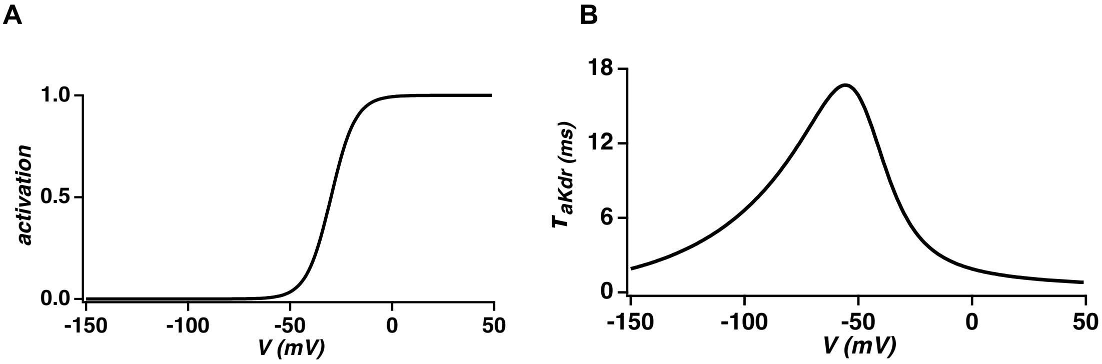

Figure 2.9. Sodium persistent channel kinetics (A) shows activation ($n_{\infty Kdr}$) probability of the delayed rectifier potassium channel with respect to voltages. (B) shows activation time constant (τ_{nKdr}) of the delayed rectifier potassium channel with respect to voltages.

$$\tau_{aKdr} = \frac{fac*1}{qt(\alpha_a+\beta_a)} \qquad (47)$$

$$\alpha_a = -0.028 * -6(1 - \frac{V-35}{\frac{-6}{2}}) \qquad (48)$$

$$\beta_a = 0.1056\, exp^{-\frac{v+60}{40}} \qquad (49)$$

qt =1

Where,

α_a, β_a are rates of transitions of open to close and vice versa of Kdr channel. τ_{aKdr} is the time constants of the channel activation. $a_{\infty Kdr}$ is the function that produces the voltage dependent activation probability. $V_{a1/2Kdr}$ is the value of voltage at which activation or inactivation of a channel is 50% where as k_{aKdr} is the factor that defines the slope of $a_{\infty Kdr}$ the activation probability curve.

2.2.7. Calcium Activated Small Conductance Potassium Channel (CaSK)

These channels are found in preBötC (Zavala-Tecuapetla et al., 2008) but no one has characterized it in preBötC. We taken the model from (Mishra and Narayanan) and tuned it according to (Ashhad and Narayanan, 2013)

$$I = \bar{g}_{CaSK} a^2 (V_m - E_k) \qquad (50)$$

$$\frac{da}{dt} = \frac{a_{\infty CaSK} - a}{\tau_{aCaSK}} \tag{51}$$

$$a_{\infty} = \frac{1}{1 + exp^{\frac{loglog\,(fq)\,-log(Cai)}{0.7651}}} \tag{52}$$

$$\tau_a = \frac{fac}{\alpha_a + \beta_a)} \tag{53}$$

$$\alpha_a = \frac{0.00246}{exp^{\frac{12log10(Cai)-28.48}{-4.5}}} \tag{54}$$

$$\beta_a = \frac{0.006}{exp^{\frac{12log10(Cai)-60.4}{35}}} \tag{55}$$

fq = 4.1676e-3

fac =1

2.2.8. Calcium Activated Cation Non-Specific Channel (CAN)

These channels are found in preBötC (Elsen and Ramirez, 1998) but have not been characterized yet. We have constructed the channel and tuned it according to (Ashhad and Narayanan, 2013)

$$I = \bar{g}_{CAN} a(Ca_i)(V_m - E_{CAN}) \tag{56}$$

$$a(Ca_i) = \frac{1}{1 + exp^{\frac{Cai-0.002}{-0.00005}}} \tag{57}$$

E_{CAN}=0

2.2.9. Calcium mechanism

Internal calcium dynamics is determined by influx of calcium through Voltage Gated Calcium Channel (VGCCs) and various efflux processes. This mechanism is adapted from (Destexhe et al., 1993). Calcium enters through VGCCs in a thin shell beneath a membrane, calcium retrieval consists of multiple process such as buffers, calcium efflux due to pump and diffusion in subsequent shells. In this mechanism as given by (Destexhe et al., 1993), calcium influx is into the thin shell beneath the membrane, and active calcium pump is implicated.

Where influx into the thin shell is

$$\frac{dCa_i}{dt} = k(\frac{i_{Ca}}{2*F*d}) \tag{58}$$

$\mathrm{d} = 0.1\ \mu m$ is the depth of the shell beneath the membrane
$\mathrm{F} = 96489\ Cmol^{-1}$ is the Faraday constant
$\mathrm{k} = \frac{1000}{18}$ is the unit conversation constant for VGCC's in $\mu A/cm^2$ and $[Ca_i]$ in millimolar.
$\mathrm{i_{Ca}}$ is the current through VGCC's
Whereas the pump kinetics are as follow

$$\frac{dCa_i}{dt} = k\left(\frac{i_{Ca}}{2*F*d}\right) + \frac{Ca_{i\infty} - Ca_i}{\tau_{Cai}} \tag{59}$$

$\tau_{\mathrm{Cai}} = 160\ ms$ is the rate of calcium removal.
This pump the calcium out unidirectionally.

These are the eight ion channels and calcium mechanism we have used to make a biophysical model of preBötC Type-1.

2.3 Multi Parametric Multi Objective Stochastic Search (MPMOSS)

It is a stochastic search strategy spanning multiple model parameters that satisfy multiple constraints on physiological measurements (Rathour and Narayanan, 2012)(Prinz et al., 2004). This strategy ensures that we are not biased toward hand-tuned models and are in the physiological ranges.

Multi Parametric (A Model with Multiple Parameters): The strategy spans multiple model parameters. This indicates that it considers several parameters simultaneously. This is beneficial where the interaction between parameters is crucial for achieving the desired outcomes. In this study, we employed 24 parameters (Table 1). A parameter is picked randomly from the uniform distribution of the parameter range.

Multi-Objective (Multiple Constraints on Physiological Measurements): Takes into account multiple constraints related to physiological measurements. This suggests that the algorithm aims to find solutions that satisfy multiple model parameters and physiological constraints. This is important where models should align with real-world physiological observations.

Stochastic Search Strategy:

- Stochastic search methods use randomness to explore the solution space (Multiple parametric ranges).
- It is helpful because we do not know the combination of parameters that can give rise to the desired phenotype.
- There might also exist degeneracy and heterogeneity. Which this method is helpful in encapsulating.

Significance: This search strategy ensures that the optimization process is not biased towards hand-tuned models. Hand-tuning involves manually adjusting model parameters, and bias toward such models can limit exploring the physiological parametric space. Given the large number of free parameters (24), hand-tuning can be exhausting.

This search strategy, MPMOSS (Mishra and Narayanan), aims to provide a more objective and automated approach to get the desired model/results.

2.4 Parametric Ranges

Experimental data for ion channels taken from literature which report mean ± SD or SEM; for our stochastic search, we have taken these ranges to create the uniform distribution, and sampling from these distributions gives the stochasticity and heterogeneity in all the models we have constructed.

$\bar{g}\ \ S/cm^2$ represents the maximum conductance

$V_{1/2}\ \ mV$ represents the voltage of half maximum activation/inactivation probability.

$\tau\ \ ms$ represents the activation/inactivation time constant of an ion channel

$Diam\ \mu m$ is the diameter of the single compart model

$R_m\ \Omega/cm^2$ is the membrane resistance per unit area

$C_m\ \mathrm{C}/cm^2$ is the capacitance per unit area

Table 1 Parametric Ranges

No.	Variables	Ranges	Unit	Reference
1	$\bar{g}_{Na}$	0.05, 0.2	S/cm^2	Optimized in this study
2	$\bar{g}_{Kdr}$	0.1, 0.6	S/cm^2	Optimized in this study
3	$\bar{g}_{ka}$	0.005, 0.05	S/cm^2	Optimized in this study
4	$\bar{g}_{Nap}$	5e-5, 4e-4	S/cm^2	Optimized in this study
5	$\bar{g}_{CaL}$	0.00007, 0.001	S/cm^2	Optimized in this study
6	$\bar{g}_{CaT}$	0.00008, 0.001	S/cm^2	Optimized in this study
7	$\bar{g}_{CAN}$	0.00004, 0.0005	S/cm^2	Optimized in this study
8	$\bar{g}_{CaSK}$	0.006, 0.06	S/cm^2	Optimized in this study
9	R_m	5000,25000	Ω/cm^2	Optimized in this study
10	$Diam$	15, 30	μm	(Koizumi et al., 2013)
11	C_m	0.8, 1.2	C/cm^2	
12	$V_{1/2aNa}$	-40.9, -34.9	mV	(Rybak et al., 2003)
13	$V_{1/2aKdr}$	-30.2, -40.2	mV	
14	$V_{1/2aKA}$	-10.3, -20.3	mV	(Hayes et al., 2008)
15	$V_{1/2aNap}$	-50.7, -40.7	mV	(Yamanishi et al., 2018)
16	τ_{aNap}	2.1, 5.1	ms	(Yamanishi et al., 2018)
17	τ_{iNap}	228, 913	ms	(Yamanishi et al., 2018)
18	$V_{1/2iNap}$	-35, -45	mV	(Yamanishi et al., 2018)
19	$V_{1/2iKA}$	-70.2, -80.2	mV	(Hayes et al., 2008)
20	τ_{iKA}	80, 353	ms	(Hayes et al., 2008)

21	τ_{aKA}	2.9, 5.8	ms	(Hayes et al., 2008)
22	τ_{aNa}	0.25, 0.875	ms	(Rybak et al., 2003)
23	τ_{iNa}	24.6, 73.8	ms	(Rybak et al., 2003)
24	τ_{aKdr}	8.78, 16.687	ms	
	Constant Variable	**Value**		
1	$V_{1/2iNa}$	-67.5	mV	(Rybak et al., 2003)
2	k_{iNa}	10.8		(Rybak et al., 2003)
3	k_{aNa}	6		(Rybak et al., 2003)
4	k_{aKA}	14.9		(Hayes et al., 2008)
5	k_{iKA}	-13.8		(Hayes et al., 2008)
6	k_{aKdr}	7.9796		
7	k_{aNap}	4.3		(Yamanishi et al., 2018)
8	k_{iNap}	-9.5		(Yamanishi et al., 2018)

2.5 Physiological measurement Ranges

We used experimentally reported measurement values of Type-1 phenotype of preBötC. each measurement are as follows:

Input resistence (R_{in}): It is defined as the gain of the neuron; it is measured as the deflection in membrane voltage at some current. It can affect how a neuron responds to synaptic input and influence its membrane potential.

Membrane time constant (τ_m): It is the time it takes for the membrane potential of a neuron to reach approximately 63.2% of its final value in response to a step change in current. membrane time constant reflects the membrane's ability to integrate synaptic input and membrane charging or discharging.

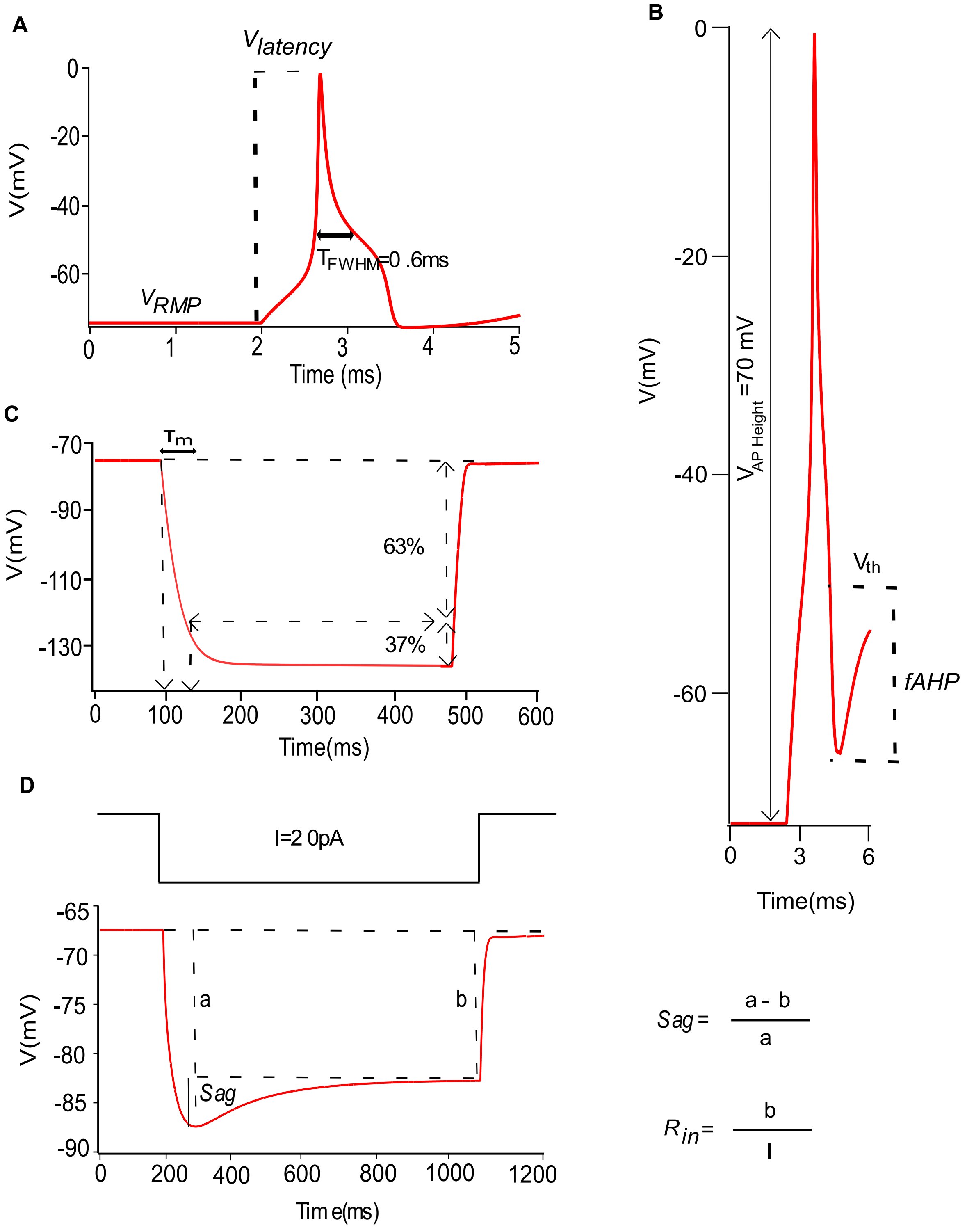

Figure 2.10 Measurement illustration (A) shows latency, FWHM and RMP of a neuron. (B) show action potential height, threshold and fAHP of a neuron. (C) shows tau of a neuron (D) shows the calculation of sag and input resistance.

Full width at Half Maxima(FWHM): It is the width of an action potential at half of its maximum value.

Threshold: It is the voltage at which an action potential initiates and if this threshold is crosed, the action potential cannot be stopped.

fast After Hyperpolarization ($fAHP$): It is calculated as the difference between threshold and the minimum point after hyperpolarization.

Resting Membrane Potential (RMP): It is the membrane potential of the neuron when it is not receiving any input.

Action Potential Height ($AP\ Height$): It is the difference between the resting state and the maximum height of the action potential.

Latency: It is the time delay between the stimulus given and the occurrence of the first spike.

Table 2 Measurement Table

No.	Measurements	Range	Unit	References
1	R_{in}	150, 1200	$M\Omega$	(Reckling et al., 1996) (Ramirez and Peter Elsen1998; Picardo 2013) (Ashhad and Feldman, 2020)
2	τ_m	5, 70 ms	ms	Picardo 2013; Sufyan and Feldman 2020
3	Sag	< 10	%	
4	$Fwhm$	< 3	ms	Del Negro et al., 2008
5	$Threshold$	-45, -60	mV	
6	$fAHP$	< 25	mV	(Zhao et al., 2006)
7	Rmp	-50, -70	mV	
8	$AP\ Height$	> 65	mV	Del Negro et al., 2002; Del Negro et al., 2002; Zhao et al., 2006
9	$Latency$	100,500	ms	Picardo et al., 2013

2.6 Making a preBötC Type-1 using MPMOSS

- **Construct a single compartment** model which would be equivalent to a soma of the neuron.
- **Create uniform distribution,** for all 24 parameters, create 24 uniform distributions with respective physiological parametric ranges reported in the literature (Table 1).
- **Stochastic Search,** From these distributions pick values randomly (black line in figure 2.11) and put that values into ion channels and ion channels into compartment model made in step1.

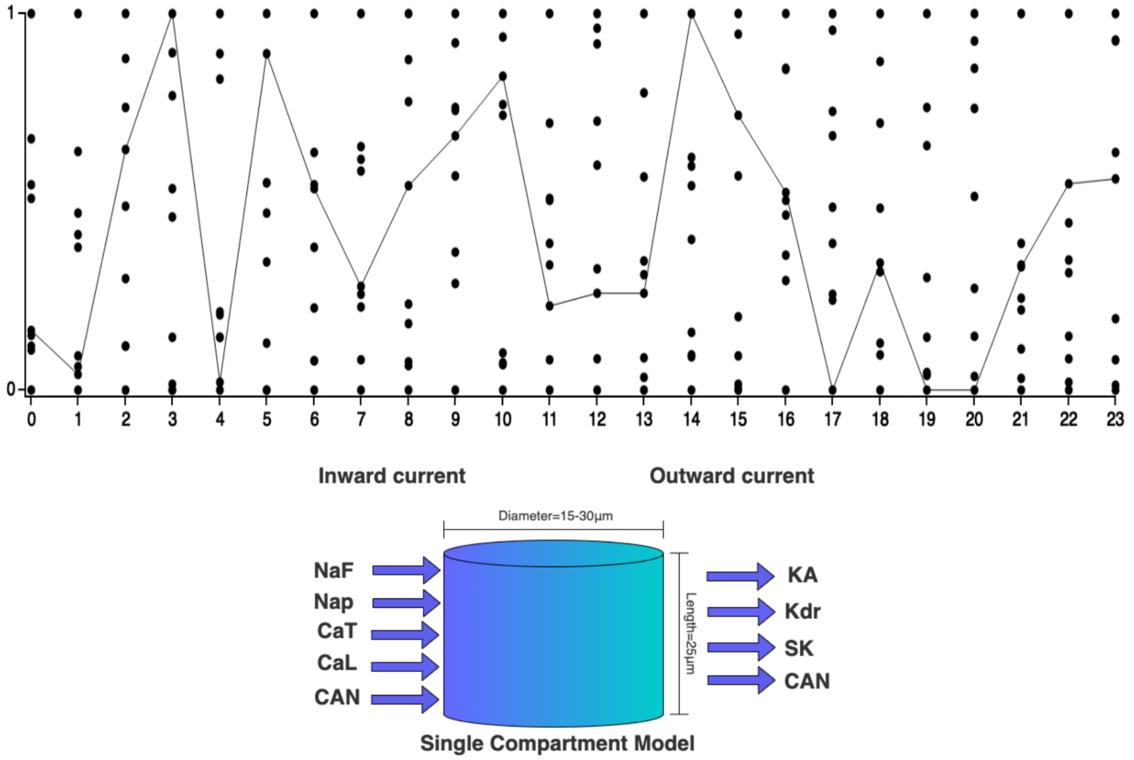

Figure 2.11 normalized uniform distributions of 24 parameters. x axis represents the parameters number . The y axis represents the normalized values of the parameter of neural model drawn from uniform distributions of each parameter. black line represents one of the model values which can construct a neuronal model.

One compartment model of the Type-1 neuron. one compart model with defined diameter, length and ion channels. with inward current by sodium fast channel (NaF), sodium persistent (Nap), Calcium captivated T type channel (CaT), Calcium activated L type channel (CaL), Calcium activated cation non-specific channel (CAN) and outward current via A type potassium channel (KA), Delayed rectifier potassium channel (Kdr), Small conductance potassium channel (SK), Calcium activated catio non-specific channel (CAN).

- **Assess the validity,** The next step is to inject sub- and supra-threshold current injections into the above compartment model and measure its active (latency, Spike Height, Threshold) and passive (Rinput, Sag, Tau) properties.
- **Analyze,** Check if measured values fall in the same range in the type-1 preBötC physiological measurements (measurements table) reported in the literature. If it qualifies all measurement ranges, it is a valid model. further analyze is in chapter 3, Results.

2.7 Simulations and analysis

Simulations performed in NEURON software with custom written code. With temperature 34°C, E_k=-70 (9mM extracellular potassium), time step 0.025 ms. Data analyzed in Igor Pro with custom written code. FWHM is not characterized in preBötC neurons. We estimated the FWHM from the voltage traces reported in the literature (Del Negro et al., 2005; Hayes et al., 2008) using the website graphreader.com. The experimental values for AP_{FWHM} , and AP_{Height} were estimated from the action potential traces Type-1 neurons reported in Table 4.

Chapter 3

Results

Table 3

No	Ion channel	Region	V1/2 Activation	V1/2 Inactivation	Tau Activation	Tau Inactivation	References
1	Sodium fast	Hippocampus (Pyramidal)	-23.9±0.9 mV	-62.9 ±1.7 mV	0.16 ± 0.02 ms	0.20 ±0.02 ms	Martina & Jonas 1997
		preBötC	–43.8 ± 2.3 mV	–67.5 ±3.6 mV	0.9 ± 0.2 ms	35.2 ± 3.4 ms	Rybak 2003
2	A-type	Hippocampus (Pyramidal)	-13 mV	-56 mV	1 ms	Linear with V, slope 2.6 ms per 10mV	(Hoffman et al., 1997)
		preBötC	-16.3 mV	-85.6 mV		200 constatnt	(Hayes et al., 2008)
3	Nap	Hippocampus (Pyramidal)	–43 ± 0.9 mV		2 ms	100 ms	Ceballos 2017
		preBötC	-47.7±2.5	-39.1±2.9	3.4±1	571±50.9	Yamanishi 2018
4	T-type	Hippocampus	-60.7, -51.7, -43.5 mV	-93.2,-85.4, -73.9 mV	20, 4, 5 ms	375, 55, 60 ms	E McRory 2001
		preBötC	-59.05±0.01	-80.72±0.14			Elsen and Ramirez 1998

This study aims to gain physiological and mechanistic insights into preBötC synchronization. preBötC synchronization is an emergent network property (Ashhad et al., 2022; Del Negro et al., 2018) shaped by intricate interactions between neuronal properties and network connectivity. Therefore, to construct preBötC network models, we first needed to build biophysical models of Type-1 preBötC neurons, which are putatively rhythmogenic to faithfully capture their properties recorded in experiments. In this endeavor, we realized that the voltage-gated ion channel (VGIC) properties in preBötC neurons differ significantly from similar ionic currents in other brain regions. For instance, the $V_{1/2}$ of activation sodium fast (Naf) currents in hippocampal CA1 pyramidal neurons is -23.9 mV (Martina and Jonas, 1997), whereas in preBötC neurons, it is -43.8 mV (Martina and Jonas, 1997). The *A*-type potassium current's inactivation is fast. It follows a linear voltage-dependence, whereas it is voltage-independent with a very slow inactivation time constant of ~250 ms in preBötC Type-1 neurons. **Table 3** summarizes such differences in the preBötC VGIC compared to the well-studied hippocampal pyramidal neurons. Such stark differences in VGIC properties rendered the readily available models of VIGCs inaccurate for construction of preBötC neuronal models. Thus, based on an extensive literature search, we first constructed the ion channel models specific to preBötC neurons (see METHODS).

We incorporated eight voltage-gated ion channels in the models of Type-1 neurons, as described in the methods, based on their characterization and the evidence of their presence from pharmacological experiments in the preBötC (Del Negro et al., 2005; Hayes et al., 2008; Rybak et al., 2003; Yamanishi et al., 2018; Zavala-Tecuapetla et al., 2008). The literature on preBötC VGICs is sparse, and not all the eight ion channels are fully characterized. Since this is the first study to construct ion channels and a biophysical model of preBötC neurons that can replicate experimentally observed measurements, we had to search wide parametric space for VGICs to arrive at ranges that could reproduce the preBötC Type-1 phenotype. For this, we optimized nine parameters for the final analysis, which include $\bar{g}_{Na}$, $\bar{g}_{Kdr}$, $\bar{g}_{ka}$, $\bar{g}_{Nap}$, $\bar{g}_{CaL}$, $\bar{g}_{CaT}$, $\bar{g}_{CAN}$, $\bar{g}_{CaSK}$, $and\ R_m$; where $\bar{g}_x$ represents the maximal conductances of Na fast, *A-type* K^+ , persistent sodium, *L-type* Ca^{2+}*,* *T*-type Ca^{2+}*-activated cation-nonspecific, and* Ca^{2+}*-activated small conductance* K^+ *channels, respectively, and* R_m *is the specific membrane resistivity.* For the remaining parameters, we took their ranges around the mean values reported in the literature **(Table1).**

We simulated ~2,00,000 models for the initial search to optimize these parametric ranges. With these optimized ranges, we constructed 90,000 models, out of which 135 models had their physiological measurements within the experimental bounds (Table 4) and, thus, qualified as valid. The low success rate of valid models (0.15%) indicates that our search strategy was unbiased towards any hand-tuned parametric range.

The histograms of various physiological measurements of the valid models captured the experimentally observed heterogeneity of preBötC Type-1 neurons (Figure 3.1). **Table 4** compares valid models' measurement ranges with the experimental estimates of sub-and supra-threshold measurements. Specifically, we analyzed nine physiological measurements that include input resistance (R_{in}), membrane charging/discharging time constant (τ_m*), sag potential (Sag (%), action potential full-width at half-maximum duration (AP_{FWHM}), action potential threshold ($AP_{threshold}$), the fast afterhyperpolarization potential following the first action potential in (AP_{fAHP}), Action potential peak (AP_{Height}* (mV) , latency to first action potential at the rheobase current injection, and the resting membrane potential(*RMP*). preBötC Type-1 neurons are characterized by a high latency to fire an action potential at rheobase current injection. Our models captured the entire range of latencies observed experimentally

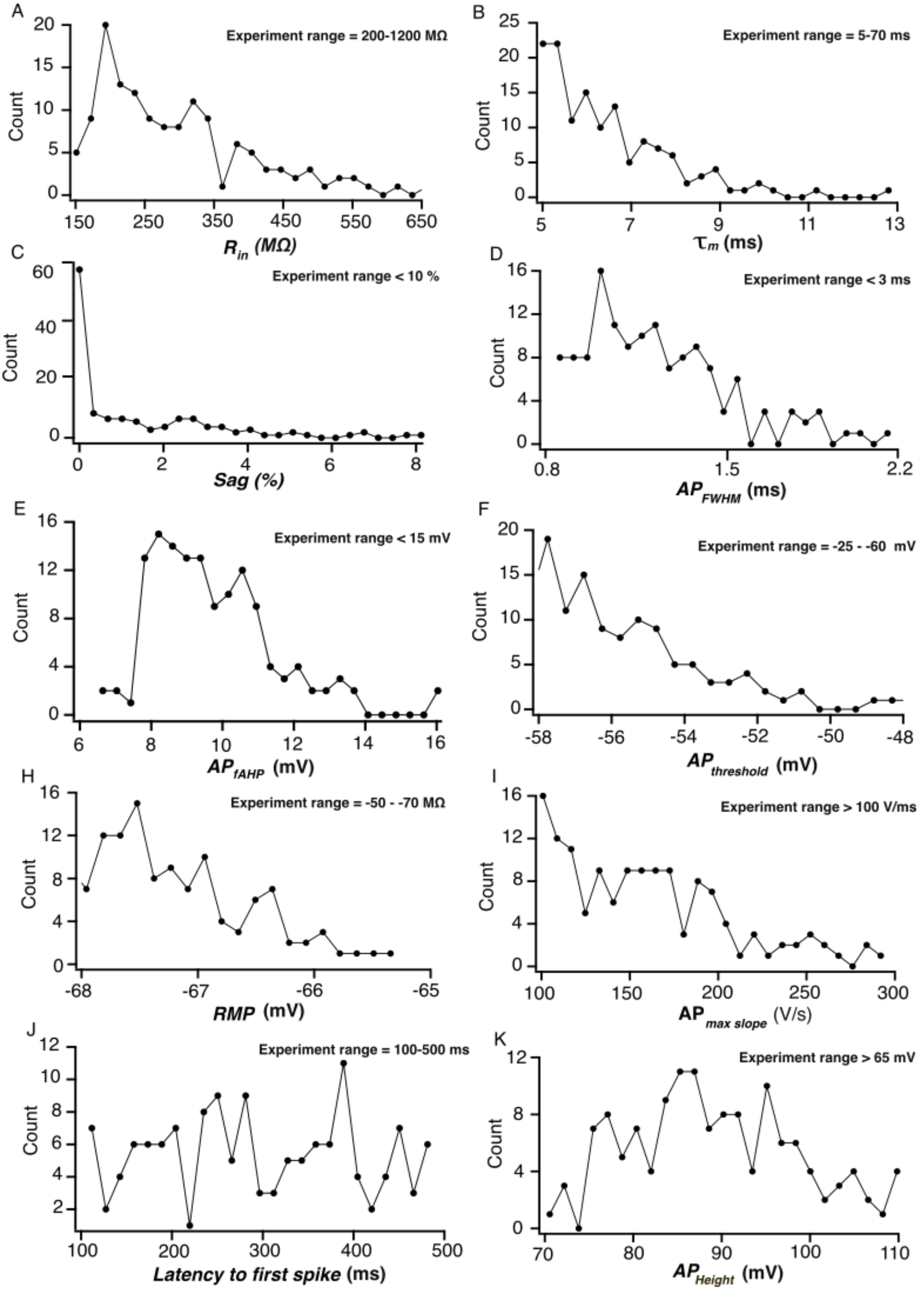

Figure 3.1 Heterogeneity in the measurements for valid models of preBötC Type-1 neurons. Histograms of (A) input resistance (R_{in}) (B) membrane charging time constant (τ_m) (C) Sag potential (D) Full-width-at-half-maximum duration of action potential (AP_{FWHM}) (E) action potential threshold ($AP_{threshold}$) (F) action potential fast after-hyperpolarization (AP_{fAHP}) (G) resting membrane potential (RMP) (H) maximum slope of action potential ($AP_{max\ slope}$) (I) Latency to first spike (J), and the amplitude of the first action potential at rheobase current injection.

Table 4 Models and experimentally reported measurements statistics

Measurement (Unit)	Experiment	Model	Reference
R_{in} $(M\Omega)$	308±38(Mean ±SEM) 306±130(Mean±SD) Range: 150, 1200	303±110(Mean±SD) Range: 155, 679	(Picardo et al., 2013; Rekling et al., 1996)
τ_m* (ms)	24 ± 3 (mean±SEM) Range: 5,70	6 ± 0.1(mean±SEM) Range: 5,13	(Ashhad and Feldman, 2020; Picardo et al., 2013)
Sag (%)	Negligible	Range: 0, 8.4	
AP_{FWHM}# (ms)	estimated: 1.3, 2.6	Range: 0.8, 2.2	(Hayes et al., 2008; Morgado-Valle and Feldman)
$AP_{threshold}$ (mV)	Not characterized	Range: -59.7, -47	
AP_{fAHP} (mV)	10.4 ± 2.8(mean±SD)	9.9 ± 1.7(mean±SD)	(Zhao et al., 2006)
Rmp (mV)	Not characterized	Range: -68.8, -65.2	
AP_{Height} † (mV)	75,58,59,51 (estimated)	Range: 70.5, 111.5	(Del Negro et al., 2005; Hayes et al., 2008; Morgado-Valle and Feldman; Zhao et al., 2006)
$Latency\ to\ first\ spike$ (ms)	308 ± 16(mean±SEM) 398± 102(mean±SD) Range: 100,500	303±9.4(mean±SEM) Range:100,500	(Picardo et al., 2013; Rekling et al., 1996)

τ_m* experimental range is taken from Dbx1+ neurons.

AP_{FWHM}# calculated from Type-1 neuron Figure 7 (Hayes et al., 2008) using a website graphreader.com.

$AP_{Height}{}^{\dagger}$ calculated from figure 6, figure 7, figure 3, figure 4 from Del Negro et al., 2005; Hayes et al., 2008; Zhao et al., 2006; Morgado-Valle and Feldman 2002 respectively using graphreader.com.

(100 ms – 500 ms). τ_m the experimental range for DBx1+ neurons was used as the reference, since Type-1 neuron specific measurements are not available. We observed that $\tau_m$does not cover the whole range of reported values because Dbx1$^+$ neurons include both Type-1 and Type-2 neurons (Picardo et al., 2013). Given that Type-2 (SST$^+$) neurons have a higher range of τ_m (10- 60 ms ; Ashhad and Feldman, 2020), our study predicts that the Type-1 neurons have small membrane time constants. Sag potential was negligible, with 60% of the models having less than 2% sag. This is consistent with experimental observations (David et al., 2022; Kallurkar et al., 2022). These measurements also fall within the experimentally determined values. For the characterization of valid models, we observed that the $AP_{threshold}$ was a critical parameter. Specifically, several models qualified all other measurement criteria but exhibited very high $AP_{threshold}$, in non-physiological ranges (up to -25 mV).

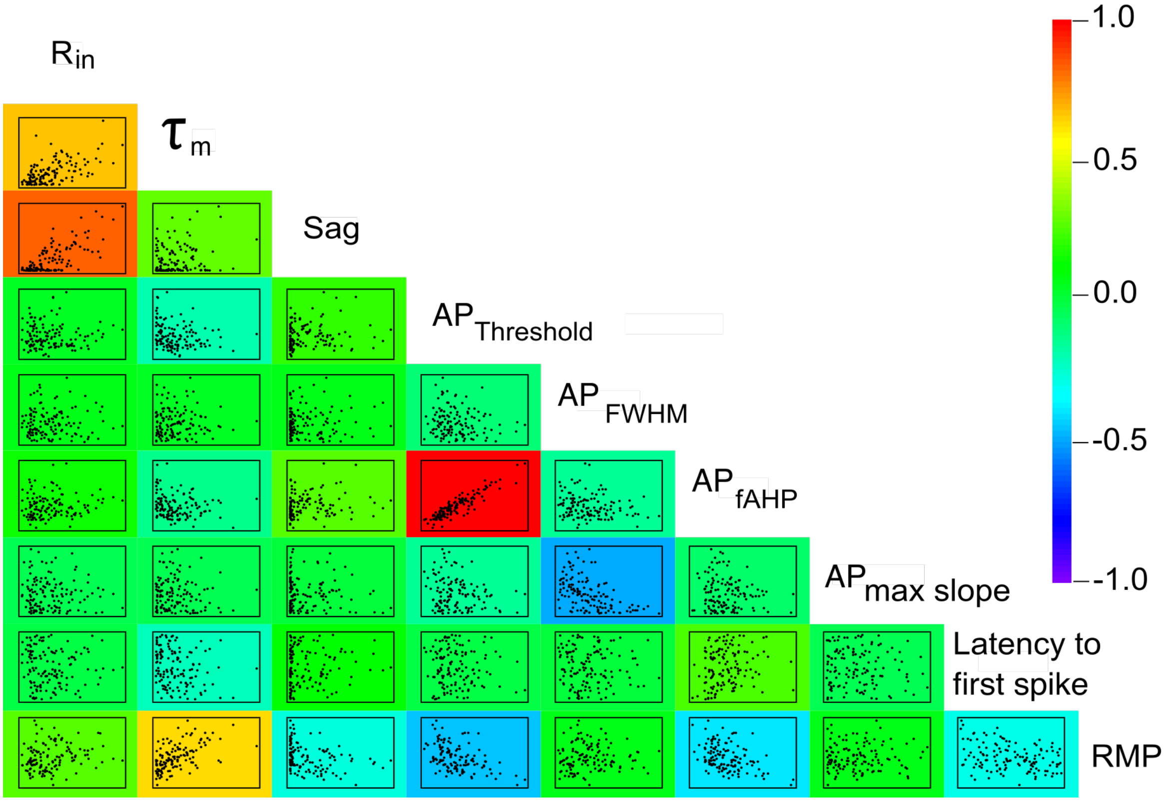

Figure 3.2 Pairwise correlation and scatter plot of all measurements of the 135 valid models (A) Pairwise scatter plot of 9 measurements. Each box is the scatter plot between the two measurements for with the background color of each plot representing the correlation strength of the two parameters. Heatmap: correlation coefficient.

Given these observations we had to fix a robust criterion for the $AP_{threshold}$ to qualify the models as valid. However, $AP_{threshold}$ for preBötC Type-1 neurons has not been characterized experimentally. Thus, we decided to fix $AP_{threshold}$ cut off to be less than -45 mV, based on the measurements from other neuron types . For the valid models $AP_{threshold}$ was between –60 to –47 mV.

Our model measurements were heterogeneous, we questioned whether these measurements held some pairwise correlation and were stilling lead to heterogeneous population. We proceeded by checking for any existing correlation and this indeed turn out to be the case (Figure 3.2). We observed that most measurement pairs (32 out of 36) were weakly correlated, reflecting a true heterogeneity in the models. Four out of 36 pairs were strongly correlated. For instance, positive correlation between $AP_{threshold}$ and AP_{fAHP} is evident because AP_{fAHP} was measured as the difference of action potential minima from the $AP_{threshold}$. Thus, greater the depolarised/hyperpolarized $AP_{threshold}$ the higher/lower the AP_{fAHP}becomes respectively. A positive correlation between R_{in} and τ_m, can be due to τ_m being proportional to R_m. $\tau_m = R_m * C_m$ and $R_{in} = R_m/area$ which makes this correlation more evident. There was a positive correlation between R_{in} and Sag, though the absolute sag is insignificant. This correlation is indirect, membrane charging (τ_m) and slow inactivation dynamics of *A-type channel* leading to this correlation. Slow the charging, more time for *A-type* inactivation leads to higher sag and via versa. A positive correlation between τ_m and the RMP of a neuron is related to the excitability of the neurons, which can be seen in a positive correlation between R_{in} and τ_m where R_{in} is the measure of excitability. There was a negative correlation between AP_{FWHM} and $AP_{\max slop}$, where $AP_{\max slop}$ is the maximum speed attained by the action potential. If an action potential has a higher speed, the width of the action potential would be low, and vice versa, hence the negative correlation.

Despite the heterogeneity spanning the whole measurement ranges with varying degrees (Table 4) of valid models (Table 4), all still exhibit Type-1 phenotype. We asked if some underlying parametric correlations define the Type-1 phenotype in preBötC neurons.

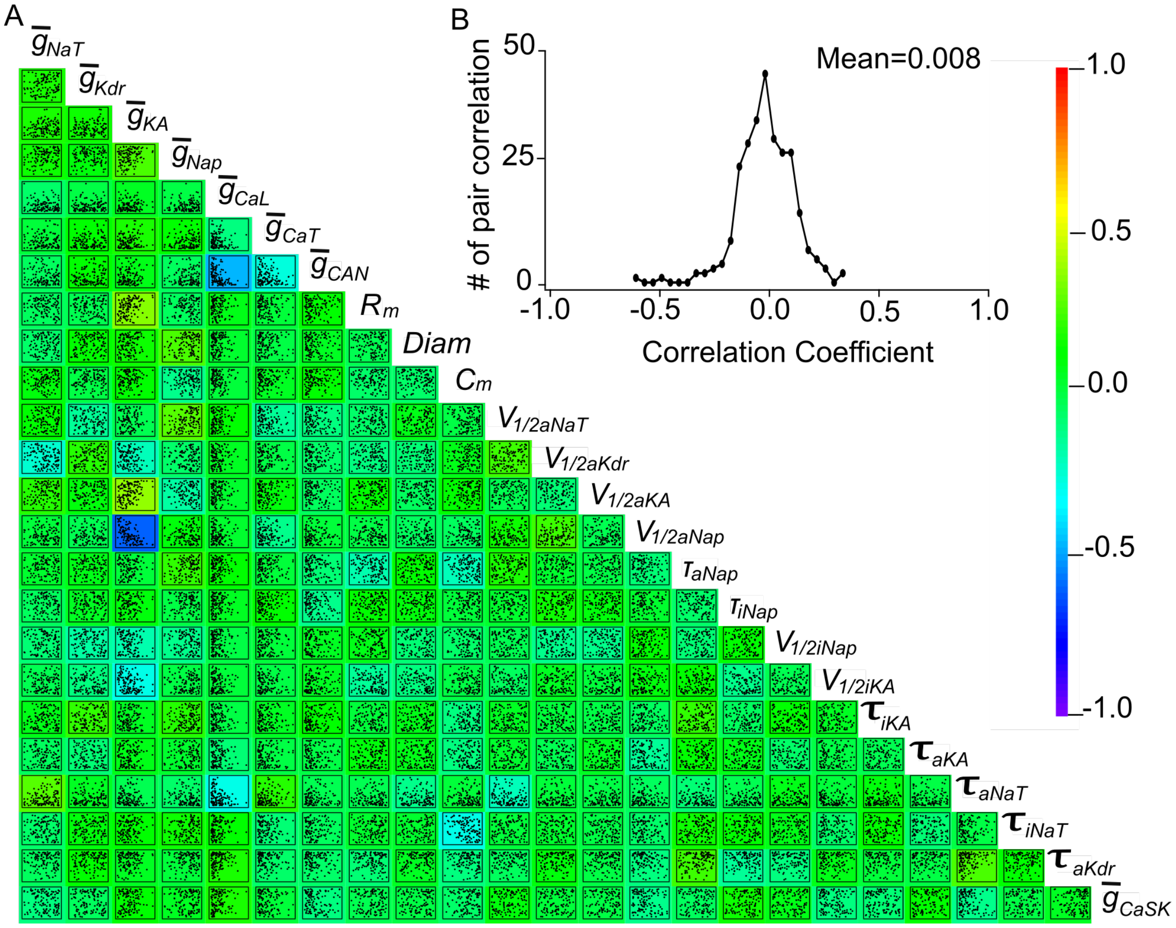

Figure 3.3 Degenerate parametric interactions underlie heterogeneity in Type-1 neuronal models. (A) Pairwise scatter and correlation plot of 24 parameters of 135 valid models. Each box is the scatter plot of two parameters, with the background color of each plot representing the correlation strength of the two parameters. Heatmap: Pearson's correlation coefficient. (B) Histogram of correlation coefficient values centered at zero, revealing weak pairwise correlations.

The valid model parameters exhibited weak pairwise correlations (Figure 3.3), with the exception of $\bar{g}_{ka}$, and $V_{1/2aNap}$ that was strongly correlated (with Pearson's coefficient of -0.6). This analysis indicates that the interactions between the sodium persistence (Nap) and A-type potassium (KA) channels might play an important role. This correlation might be essential to defining the preBötC Type-1 phenotype (Goaillard and Marder, 2021, also see DISCUSSION).

The weak correlation in underlying parameters reveals the underlying degeneracy in the model parameters, where disparate parametric interactions give rise to the Type-1 physiological phenotype. This is further evident in the parametric comparison of three example models with similar physiological measurements. Figure 3.4 shows three degenerate models with approximately the exact measurements and varying degrees of underlying parameters. For type-1 models showing heterogeneity and degeneracy, we checked whether any measurement correlated to any parameters (Figure 3.5). Latency, which is a critical measurement for Type-1 phenotype, has low correlations with all parameters. We found that multiple parameters (R_m, $Diam$, $V_{1/2aNa}$) showed a correlation with one measurement (Sag). While, multiple measurements (R_{in}, Sag, $AP_{threshold}$, AP_{fAHP}) correlate with the same parameter ($V_{1/2aNap}$). Thus,

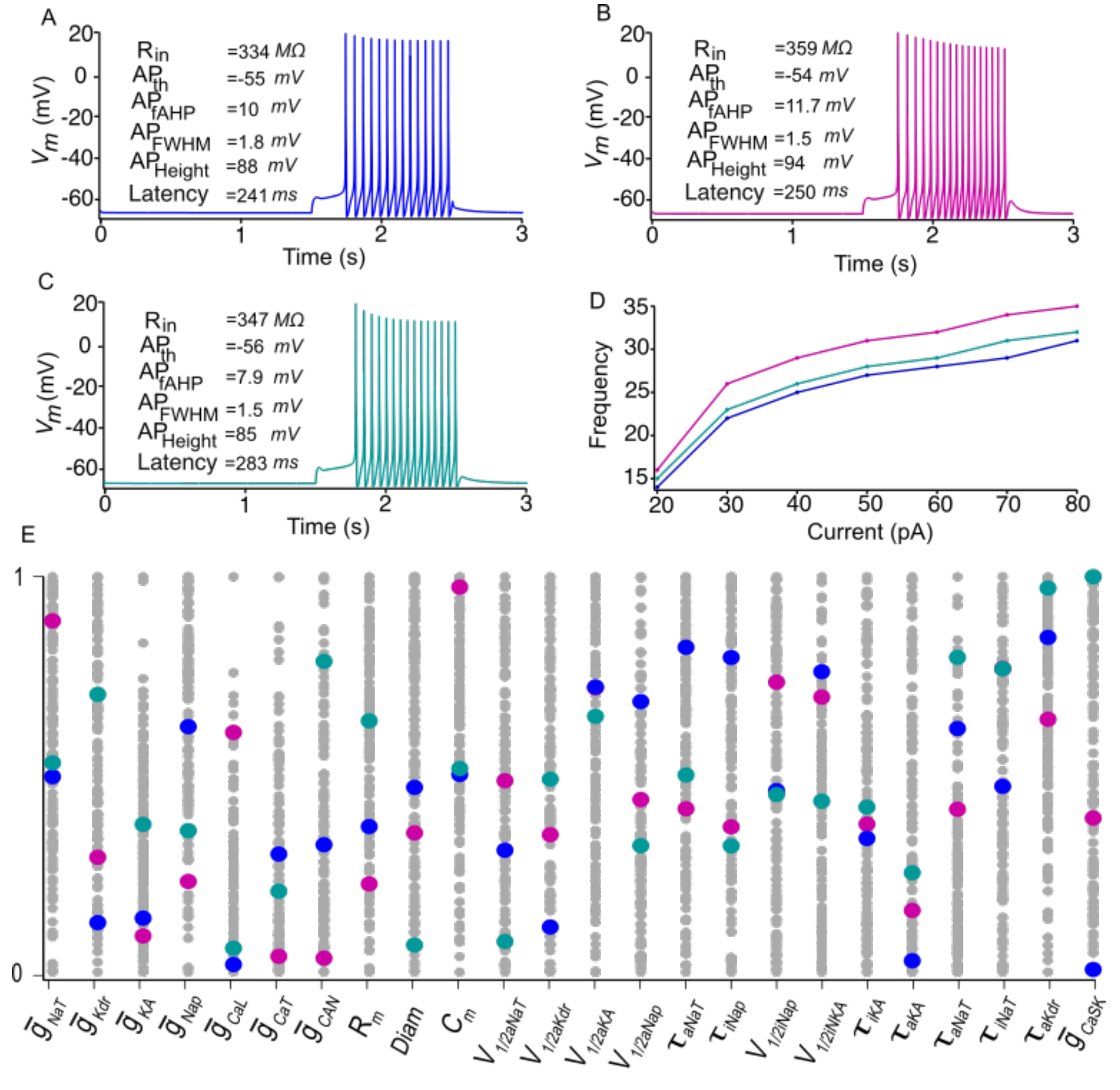

Figure 3.4 Illustration of functional degeneracy in preBötC Type-1 neuronal models. (A) Selected four valid models (in different colors) with similar physiological measurements. each neuron's corresponding measurements are indicated (B) normalized parametric ranges of 135 qualified models (grey dots). Parameters of four models (color-coded according to their traces in A) are highlighted. The underlying parametric ranges of these four models are quite different, even though their physiological measurements are similar.

there exist one-to-many and many-to-one correlations between the parameters and the measurements.

This also implies that this phenotype is not because of one parameter, but it is a combinatorial effect of multiple parameters. A few prominent correlations, τ_{aNa} and AP_{FWHM} , are highly positively correlated, which was reasonably expected. For instance, fast/slow sodium channel activation will lead to a fast/slow ramp-up of the action potential, which, in turn, will lead to small/large AP_{FWHM}, as it is also seen in Figure 3.4. R_{in} and $Diam$ are negatively correlated since, as explained above, R_{in} is inversely proportional to the neuronal surface area. R_{in} and $\bar{g}_{ka}$ are negatively correlated. A-Type potassium channel has a large window current around the resting membrane potential. Thus, around resting membrane potential, increased A-Type conductance will act as a leak conductance, decreasing the gain of the neuron (Rathour and Narayanan, 2012). There exists a positive correlation between AP_{fAHP} and $V_{1/2aNap}$. Given depolarizing conductance sodium persistent and sodium fast plays a vital role in determining the neuron's threshold. Threshold correlated to AP_{fAHP}; hence, not just $V_{1/2aNap}$ should correlate to AP_{fAHP}; we would expect sodium fast also to correlate, and it indeed correlates weekly (Figure 3.5). A negative correlation between Sag and Diam of a model does not seem to be a direct correlation; larger $Diam$ leads to lower R_{in} and hence low τ_m (a positive correlation between R_{in} and τ_m Figure 3.2) and hence less sag as explained before.

With this one-to-many and many-to-one relationship between parameters and measurements of the neuronal population, we looked at how the Type-1 neuronal population might participate in synchronization. We computed the spike-triggered average (STA) currents in ten randomly selected models out of the 135 valid ones (Das and Narayanan, 2014). We injected Gaussian white noise with zero mean and tuned the variance for each model so that the firing frequency was less than 1 Hz. We averaged the current up to 200 ms before the action potential.

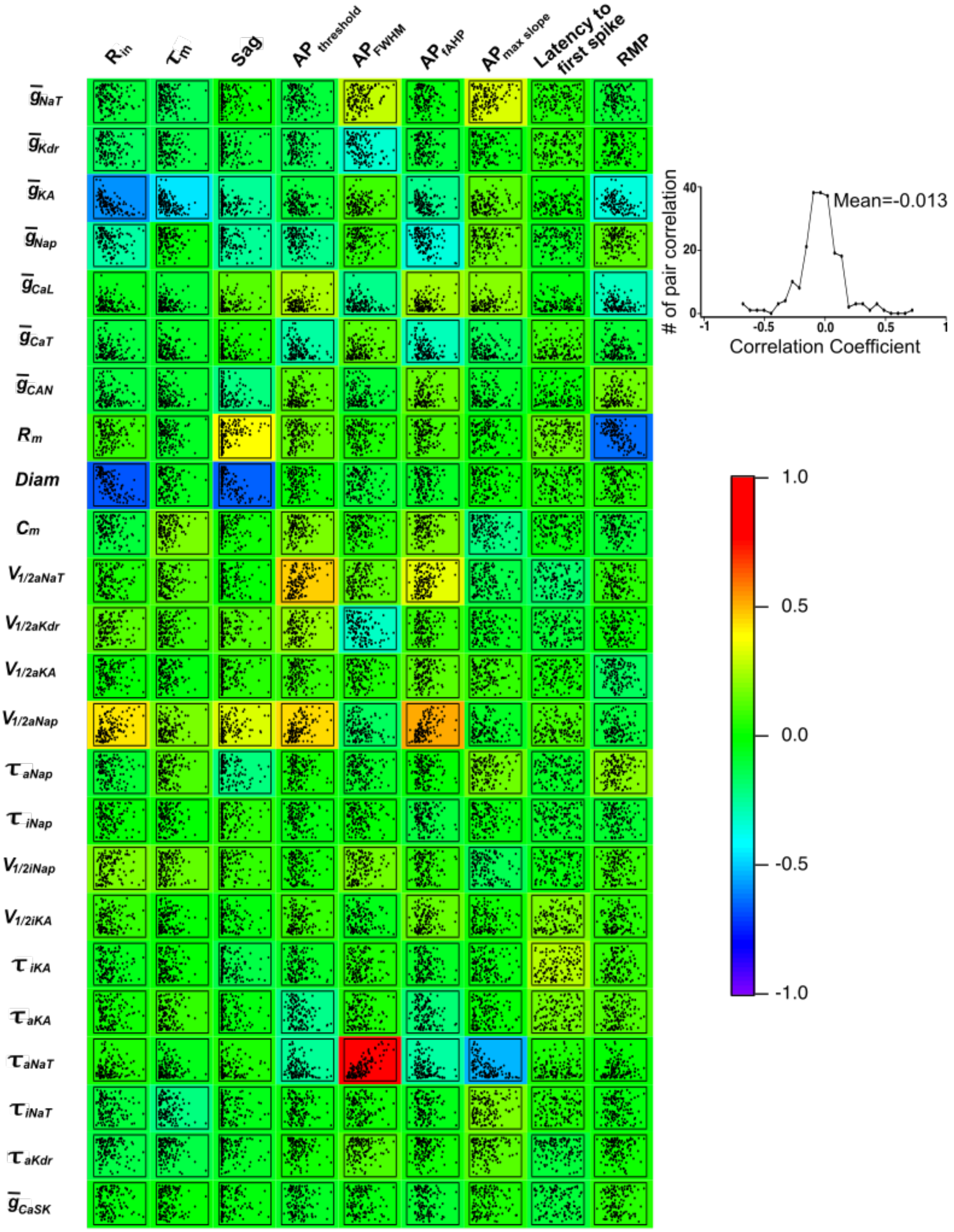

Figure 3.5 Scatter plot between parameters and measurements. Each box is a scatter plot between one parameter and a measurement; the color of the box indicates Pearson's correlation coefficient as the heat map. There are few strong correlations, whereas most pairs are weakly correlated.

This gave us insights into the current waveforms to which the neuron was optimally responsive (Figure 3.6). We observed that the neuronal population exhibited STAs, which could be qualified into the entire spectrum of integrators (model 8) to coincidence detectors (model 5) with varying degrees. The underlying parameters for these neurons were widely distributed, suggesting that the integrator- and the coincidence detector-type STAs are not associated with any specific model parameter.

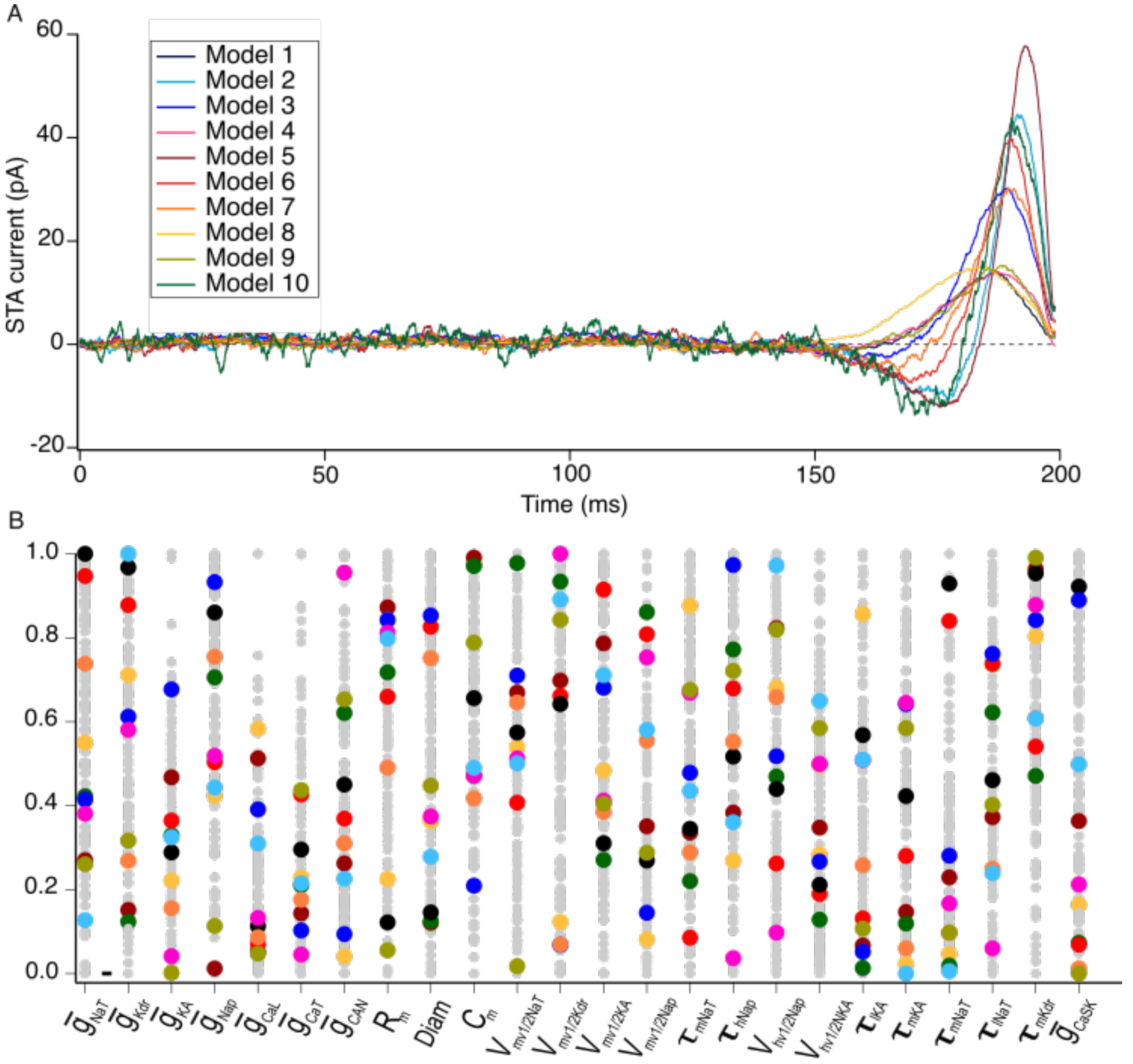

Figure 3.6 Spike-triggered average (STA) currents reveal a wide spectrum of computational regimes, from integrators to coincidence detectors, in pr.eBötC Type-1 neuronal models (A) STA analysis of 10 randomly selected valid models. The integrators (e.g., model 8) show a monophasic positive STA current up to 50 ms before the spike; differentiators or coincidence detectors (e.g., models 2,5,6, 7, and 10) exhibit a biphasic STA current with a negative current window that precedes a narrower positive currents window before the spikes. (B) These models' underlying parametric ranges do not correlate with the specific type of STAs. Note that model pairs with overlapping STAs, e.g., models 4 and 9 and models 2 and 10, lack overlapping (correlated) parametric distributions.

Chapter 4

Discussion

All valid models span the measurement ranges on which they were constrained. The model parameters were weakly correlated. Therefore, this Type-1 phenotype cannot be explained by a particular parameter; it is the interplay of all the parameters that causes the Type-1 phenotype to emerge. A pairwise comparison of model parameters and measurements revealed one-to-many and many-to-one correlations. This again implies that one physiological property (measurement) cannot be explained by any specific model component (parameter). There is an exception in our models; one prominent negative correlation comes up between $\bar{g}_{ka}$, and $V_{m1/2Nap}$. Since the lower $V_{m1/2Nap}$ results in higher Nap currents near resting membrane potential, this correlation implies that the KA and Nap channel expression is positively correlated in preBötC Type-1 neurons.

There are two possibilities: either it is a spurious correlation, or our study predicts that correlations between the KA and Nap channel define the Type-1 phenotype in preBötC. To test this prediction, we carefully screened the single-cell transcriptomics data of preBötC Type-1 and Type-1 neurons collated via patch-seq analysis (David et al., 2022). Surprisingly, this correlation can also be seen at the transcriptional level as well(Kallurkar et al., 2022). A-type current is mediated by K_v channels $K_v1.4$ $(Kcna4)$, $K_v3.3 - 3.4$ $(Kcna3 - 4)$, and $K_v4.1 - 4.3$ $(Kcnd1 - 3)$. And sodium persistent channel $(Na_v1.6)$ encoded by $Scn8a$ gene are present in preBötC Type-1. All 7 Type-1 neurons show correlated expression (Appendix) either both have high level (2th ,3th ,4th ,6th ,7th neurons from the left in pink) of expression or the low levels (1st , 5th from the left in pink) of expression. Notably, such a strong correlation was not observed in the Type-2 neurons.

A possible reason for the prominent correlation between *Nap* and *KA* is that Nap is important for depolarizing the neurons once *KA* inactivates to the activation potential of fast sodium currents. *Nap* does not inactivate completely (2.2.5) and it has a high window current. During the initial latency period, *KA* competes against sodium fast and *Nap* channels. Whereas the fast sodium current needs a certain depolarization to get activated, persistent can lead to depolarization and contribute to neuronal firing. This has to be tested via pharmacological blocking of *Nap* channels.

Type-1, the characteristic of delayed firing upon current injections, has been hypothesized to be majorly contributed by the *KA* channels. Because of its fast kinetics, *KA* currents can compete with transient sodium currents, which delays the action potential firing. Also, *KA* inactivation is time-dependent and voltage-independent in preBötC (Hayes et al., 2008). Therefore, once it starts to inactivate after a delay, trainset sodium current takes over, leading to the neuron's firing. If this is true, then the action potential latency of a neuron should correlate to *A*-type inactivation. This was observed in the measurements vs parameters pairwise correlation Figure 3.5.

Do *KA* potassium and *Nap* exclusively determine the Type-1 phenotype, or can it come about via other channel interactions, too? In future analysis, we will address this question by implementing a virtual knock-out of different VGICs and analyzing their impact on the measurements of valid models. The virtual knockout experiments of each channel one-by-one to screen for knockouts that can abolish the Type-1 phenotyp would be crucial to address this question.

Another insight from this study is on the encoding properties of the preBötC Type-1 neuronal population. Type-1 neurons are considered integrators (Prescott, 2014). However, our STA analysis on randomly selected valid models revealed that preBötC Type-1 neurons exhibit the entire spectrum from integers to coincidence detectors. This heterogeneity is useful for the network and might be important for the resilience of the network under various physiological states (Dong et al., 2018).

In this thesis, I have completed the first step of the work to construct the population. preBötC Type-1 neurons. My future experiments will involve conducting the second part of the project, connecting these neurons into networks (of excitatory Type-1 and inhibitory neurons), and uncovering the mechanistic underpinnings of preBötC rhythmogenesis.

The valid models exhibit heterogeneity in various properties, which might be vital for the network to be resilient in the face ever changing physiological demands. How do the variations in ion channels, which define neuronal properties and excitability, help the network to be resilient? The respiratory system operates under diverse physiological conditions, from tranquil breathing to the heightened demands of exercise or stress. For example, during the heightened demand, we have increased frequency of breathing with respect to resting resting state. This increase in frequency would require preBötC to synchronize and desynchronize at a faster speed. This dynamic change will require an increased neuronal activity which might cause network fatigue if all neurons were to have similar excitability. The heterogeneity in neuronal excitability, and hence their responsiveness to excitatory inputs, would ensure that network activity is not oversaturated, and the dynamic range of network output is tunable within a wider range of regulatory inputs. In the same way, computational heterogeneity in preBötC neurons may be essential to modulate preBötC dynamics in different respiratory states.

For instance, when during hypoxia/hypercapnia, there is increased rate firing of the upstream networks that process chemosensory inputs. Under these circumstances, neurons that act as integrators (as assessed through the STA) are better suited to optimally respond to the rate-modulated inputs. Whereas, under vocalization/ speech preBötC dynamics undergoes very precise temporal modulations (Okobi et al., 2019; Wei et al., 2022) where coincidence detectors are better suited to process such inputs. I am poised to explore how these variations in ion channel properties manifest during different respiratory states, thus shedding light on the dynamic nature of respiratory control.

An important finding of this study is that preBötC Type-1 neurons operate in a coincidence detector-like mode, as opposed to the conventional integrator mode. Typically, coincidence detection arises due to hyperpolarizing-activated cation nonspecific currents (HCN channels). HCN channels in neurons act as coincidence detectors because their restoring properties counteract changes in membrane potential. Interestingly, our valid models, despite lacking HCN channels, still exhibit a coincidence detector-like mode of operation. Upon investigation, we found that A-type conductance in our models shares properties with HCN channels, such as being restorative and having slow inactivation. These unique properties of A-type conductance transform the mode of operation of Type-1 neurons from integrators to coincidence detectors. Furthermore, varying the expression levels of this conductance allows neurons to switch modes based on the network's conditions and demands. This implies that different combinations of channels can lead to the same operational mode in various parts of the brain, highlighting an underlying degeneracy in neuronal mode of operation.

Understanding how variations in ion channel properties contribute to these distinct respiratory states is crucial for deciphering the adaptability and resilience of the respiratory network.

References

Abraham, K. A., Feingold, H., Fuller, D. D., Jenkins, M., Mateika, J. H. and Fregosi, R. F. (2002). Respiratory-related activation of human abdominal muscles during exercise. *J. Physiol.* **541**, 653–663.

Ashhad, S. and Feldman, J. L. (2020). Emergent Elements of Inspiratory Rhythmogenesis: Network Synchronization and Synchrony Propagation. *Neuron* **106**, 482-497.e4.

Ashhad, S. and Narayanan, R. (2013). Quantitative interactions between the A-type K^+ current and inositol trisphosphate receptors regulate intraneuronal Ca^{2+} waves and synaptic plasticity: Transient K^+ current regulates ER Ca^{2+} release. *J. Physiol.* **591**, 1645–1669.

Ashhad, S., Kam, K., Del Negro, C. A. and Feldman, J. L. (2022). Breathing Rhythm and Pattern and Their Influence on Emotion. *Annu. Rev. Neurosci.* **45**, 223–247.

Butera, R. J., Rinzel, J. and Smith, J. C. (1999). Models of Respiratory Rhythm Generation in the Pre-Bötzinger Complex. I. Bursting Pacemaker Neurons. *J. Neurophysiol.* **82**, 382–397.

Cui, Y., Kam, K., Sherman, D., Janczewski, W. A., Zheng, Y. and Feldman, J. L. (2016). Defining preBötzinger Complex Rhythm- and Pattern-Generating Neural Microcircuits In Vivo. *Neuron* **91**, 602–614.

Das, A. and Narayanan, R. (2014). Active Dendrites Regulate Spectral Selectivity in Location-Dependent Spike Initiation Dynamics of Hippocampal Model Neurons. *J. Neurosci.* **34**, 1195–1211.

David, C. K., Sugimura, Y. K., Kallurkar, P. S., Picardo, M. C. D., Saha, M. S., Conradi Smith, G. D. and Del Negro, C. A. (2022). Single cell transcriptome sequencing of inspiratory neurons of the preBötzinger complex in neonatal mice. *Sci. Data* **9**, 457.

Del Negro, C. A., Morgado-Valle, C., Hayes, J. A., Mackay, D. D., Pace, R. W., Crowder, E. A. and Feldman, J. L. (2005). Sodium and Calcium Current-Mediated Pacemaker Neurons and Respiratory Rhythm Generation. *J. Neurosci.* **25**, 446–453.

Del Negro, C. A., Funk, G. D. and Feldman, J. L. (2018). Breathing matters. *Nat. Rev. Neurosci.* **19**, 351–367.

Destexhe, A., Babloyantz, A. and Sejnowski, T. J. (1993). Ionic mechanisms for intrinsic slow oscillations in thalamic relay neurons. *Biophys. J.* **65**, 1538–1552.

Dong, G., Fan, J., Shekhtman, L. M., Shai, S., Du, R., Tian, L., Chen, X., Stanley, H. E. and Havlin, S. (2018). Resilience of networks with community structure behaves as if under an external field. *Proc. Natl. Acad. Sci.* **115**, 6911–6915.

Elsen, F. P. and Ramirez, J.-M. (1998). Calcium Currents of Rhythmic Neurons Recorded in the Isolated Respiratory Network of Neonatal Mice. *J. Neurosci.* **18**, 10652–10662.

Gray, P. A., Rekling, J. C., Bocchiaro, C. M. and Feldman, J. L. (1999). Modulation of Respiratory Frequency by Peptidergic Input to Rhythmogenic Neurons in the PreBötzinger Complex. *Science* **286**, 1566–1568.

Hayes, J. A., Mendenhall, J. L., Brush, B. R. and Del Negro, C. A. (2008). 4-Aminopyridine-sensitive outward currents in preBötzinger complex neurons influence respiratory rhythm generation in neonatal mice: Transient K^+ currents in preBötC neurons. *J. Physiol.* **586**, 1921–1936.

Hodgkin, A. L. (1948). The local electric changes associated with repetitive action in a non-medullated axon. *J. Physiol.* **107**, 165–181.

Hoffman, D. A., Magee, J. C., Colbert, C. M. and Johnston, D. (1997). K+ channel regulation of signal propagation in dendrites of hippocampal pyramidal neurons. *Nature* **387**, 869–875.

Kallurkar, P. S., Picardo, M. C. D., Sugimura, Y. K., Saha, M. S., Conradi Smith, G. D. and Del Negro, C. A. (2022). Transcriptomes of electrophysiologically recorded Dbx1-derived respiratory neurons of the preBötzinger complex in neonatal mice. *Sci. Rep.* **12**, 2923.

Koizumi, H., Koshiya, N., Chia, J. X., Cao, F., Nugent, J., Zhang, R. and Smith, J. C. (2013). Structural-Functional Properties of Identified Excitatory and Inhibitory Interneurons within Pre-Bötzinger Complex Respiratory Microcircuits. *J. Neurosci.* **33**, 2994–3009.

Martina, M. and Jonas, P. Functional differences in Nae channel gating between fast-spiking interneurones and principal neurones of rat hippocampus.

Mishra, P. and Narayanan, R. Disparate forms of heterogeneities and interactions among them drive channel decorrelation in the dentate gyrus: Degeneracy and dominance.

Morgado-Valle, C. and Feldman, J. L. Respiratory Rhythm: An Emergent Network Property?

Okobi, D. E., Banerjee, A., Matheson, A. M. M., Phelps, S. M. and Long, M. A. (2019). Motor cortical control of vocal interaction in neotropical singing mice. *Science* **363**, 983–988.

Phillips, R. S. and Rubin, J. E. (2022). Putting the theory into 'burstlet theory' with a biophysical model of burstlets and bursts in the respiratory preBötzinger complex. *eLife* **11**, e75713.

Picardo, M. C. D., Weragalaarachchi, K. T. H. and Akins, V. T. (2013). Physiological and morphological properties of Dbx1-derived respiratory neurons in the pre-Bo¨ tzinger complex of neonatal mice. *J Physiol*.

Prescott, S. A. (2014). Excitability: Types I, II, and III. In *Encyclopedia of Computational Neuroscience* (ed. Jaeger, D.) and Jung, R.), pp. 1–7. New York, NY: Springer New York.

Rathour, R. K. and Narayanan, R. (2012). Inactivating ion channels augment robustness of subthreshold intrinsic response dynamics to parametric variability in hippocampal model neurons. *J. Physiol.* **590**, 5629–5652.

Rekling, J. C., Champagnat, J. and Denavit-Saubie, M. (1996). Electroresponsive properties and membrane potential trajectories of three types of inspiratory neurons in the newborn mouse brain stem in vitro. *J. Neurophysiol.* **75**, 795–810.

Rybak, I. A., Ptak, K., Shevtsova, N. A. and McCrimmon, D. R. (2003). Sodium Currents in Neurons From the Rostroventrolateral Medulla of the Rat. *J. Neurophysiol.* **90**, 1635–1642.

Wei, X. P., Collie, M., Dempsey, B., Fortin, G. and Yackle, K. (2022). A novel reticular node in the brainstem synchronizes neonatal mouse crying with breathing. *Neuron* **110**, 644-657.e6.

Yamanishi, T., Koizumi, H., Navarro, M. A., Milescu, L. S. and Smith, J. C. (2018). Kinetic properties of persistent Na+ current orchestrate oscillatory bursting in respiratory neurons. *J. Gen. Physiol.* **150**, 1523–1540.

Zavala-Tecuapetla, C., Aguileta, M. A., Lopez-Guerrero, J. J., González-Marín, M. C. and Peña, F. (2008). Calcium-activated potassium currents differentially modulate respiratory rhythm generation. *Eur. J. Neurosci.* **27**, 2871–2884.

Zhao, M.-G., Hülsmann, S., Winter, S. M., Dutschmann, M. and Richter, D. W. (2006). Calcium-regulated potassium currents secure respiratory rhythm generation after loss of glycinergic inhibition. *Eur. J. Neurosci.* **24**, 145–154.

Appendix

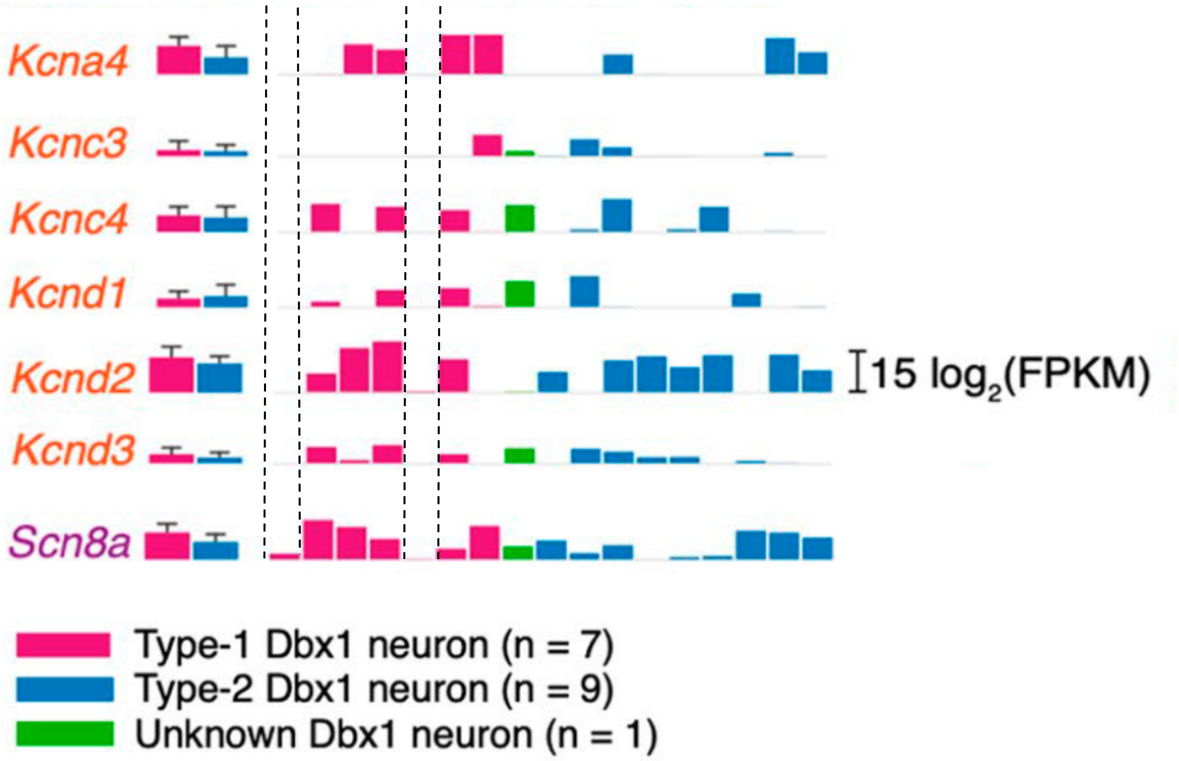

Correlation between *A*-type potassium and sodium persistent in Type-1 neuron of the preBötC at transcriptional level. Figure taken from (Kallurkar et al., 2022)